

Generative 3D Gaussians with Learned Density Control

RUNJIE YAN*, Institute for Interdisciplinary Information Sciences, Tsinghua University, China

YAN-PEI CAO, VAST, China

PENG WANG, VAST, China

DING LIANG, VAST, China

YUAN-CHEN GUO†, VAST, China

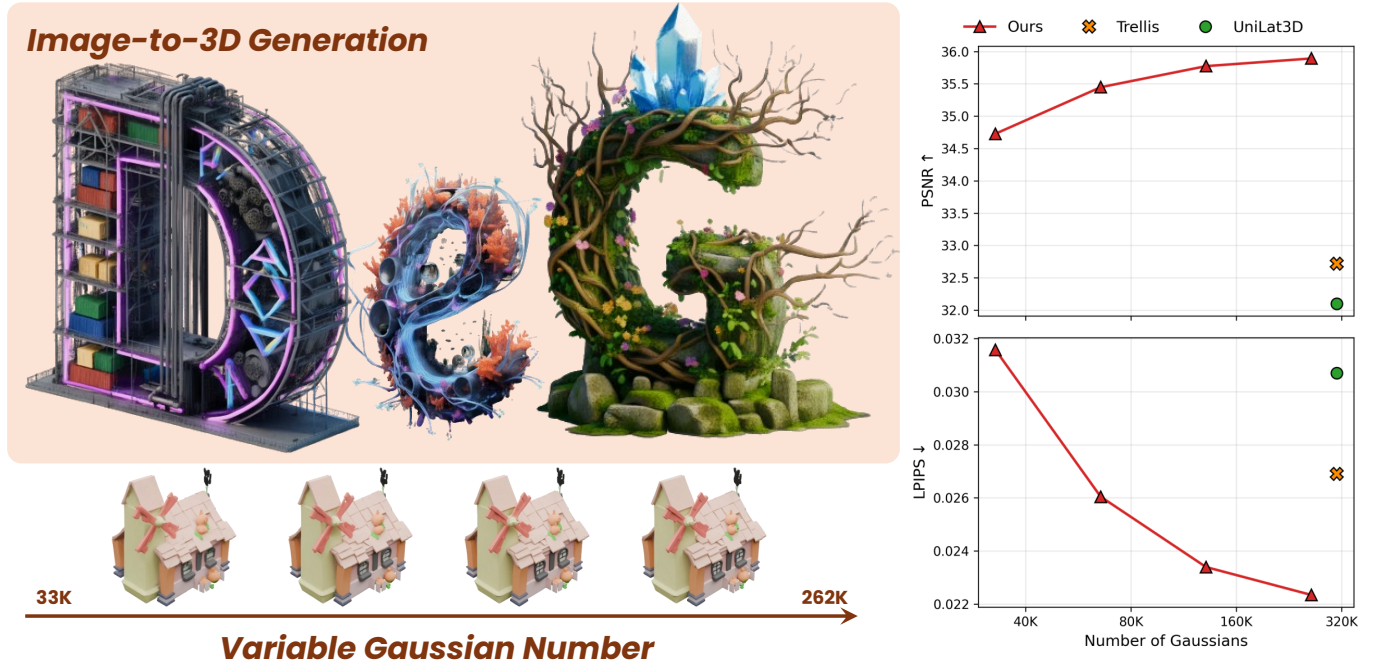


Fig. 1. Teaser. Best generation samples with variable Gaussian counts, demonstrating that our model can decode an arbitrary number of 3D Gaussian splats from a single latent representation.

We present **Density-Sampled Gaussians (DeG)**, a novel 3D representation designed to bridge the gap between adaptive rendering primitives and scalable generative modeling. Unlike existing approaches that constrain 3D Gaussians to fixed voxel grids or arrays, DeG models Gaussian centers as samples from a learnable probability density function defined over an octree. This formulation provides a rigorous mathematical framework for *adaptive density control*: by jointly optimizing the spatial density and Gaussian attributes under rendering supervision, our model naturally concentrates primitives in regions of high geometric complexity. We achieve this via a new *render loss contribution gradient* that serves as a fully differentiable analogue to the discrete densification and pruning heuristics used in standard Gaussian Splatting. The resulting representation is highly flexible, supporting *variable-resolution decoding* from a single latent code by simply adjusting the sampling budget. To enable generative synthesis, we train a latent diffusion model on DeG. We identify a critical challenge in applying diffusion to unordered set-structured latents, which can significantly slow convergence, and propose *VecSeq*, a canonical re-indexing mechanism that anchors latent tokens to a deterministic 3D Sobol sequence. This transforms the ambiguous set-generation problem into a robust sequence modeling task. Extensive

*Work done during internship at VAST

†Corresponding author

experiments demonstrate that our pipeline achieves state-of-the-art quality in single-image-to-3D generation, combining the structural adaptivity of unstructured primitives with the training stability of grid-based methods.

CCS Concepts: • **Computing methodologies** → **Artificial intelligence**.

Additional Key Words and Phrases: Generative Models, Gaussian Splatting

1 Introduction

3D generative models are increasingly central to graphics and vision, enabling content creation for AR/VR, simulation, robotics, and interactive applications. A core challenge is finding a 3D representation that is both amenable to learning and capable of high-fidelity rendering at a practical cost. Recent work has explored multiple representations for generative modeling [Poole et al. 2022; Tang et al. 2024b; Xiang et al. 2025b], seeking a favorable balance among expressiveness, efficiency, and differentiability. In this landscape, 3D Gaussian Splatting [Kerbl et al. 2023] has emerged as a compelling representation due to its flexibility, high visual quality, and promising rendering speed.

The quality of 3D Gaussians largely stems from the density control strategy [Hanson et al. 2025; Rota Bulò et al. 2024; Ye et al. 2024]. Iterative densification and pruning are performed throughout the fitting process to increase Gaussian density in under-fit regions and to remove Gaussians that contribute little. Density control allocates more Gaussians to complex regions and fewer to simple ones, striking a balance between the number of Gaussians and visual quality. However, densification and pruning are non-differentiable and difficult to vectorize, which makes them impractical in a generalizable learning setting. As a result, existing approaches to generative modeling of Gaussians typically represent a 3D scene with a fixed number of Gaussians tied to predefined structures. For example, GaussianCube [Zhang et al. 2024b] optimizes a fixed N^3 Gaussians per object and reorganizes them onto a grid using optimal transport. Structured latents [Wu et al. 2025; Xiang et al. 2025b] assign a fixed number of Gaussians to each voxel in a given sparse structure. Pixel-aligned Gaussians [Tang et al. 2024a; Xu et al. 2024; Zhang et al. 2024a] use a fixed number of Gaussians per image pixel or patch. None of these methods can adaptively allocate Gaussians based on local complexity, so they often require an excessive number of Gaussians to achieve high visual fidelity. This, in turn, complicates training and increases rendering cost.

In this work, we propose a generative framework that restores the adaptive capability of 3DGS without per-scene optimization. We introduce *Density-Sampled Gaussians (DeG)*, a representation where Gaussian centers are dynamically sampled from a learned 3D probability density function (PDF). Rather than regressing fixed coordinates, our decoder predicts a spatial distribution indicating the likelihood of surface geometry. This formulation decouples the spatial distribution of primitives from their attributes. At inference time, we can sample an arbitrary number of anchors from this density, allowing a single trained model to generate lightweight assets for mobile applications or ultra-dense assets for high-fidelity rendering simply by varying the sample count.

The primary technical challenge lies in optimizing this stochastic density end-to-end. Since the sampling operation is non-differentiable, standard backpropagation cannot update the density based on rendering error. We address this by deriving the *render loss contribution gradient*, which measures the marginal contribution of each sampled anchor to the rendering loss via the difference reward [Wolpert and Tumer 2001], and use this signal to reinforce the probability density in regions where primitives significantly reduce reconstruction error. This provides a fully differentiable alternative to the heuristic densification and pruning used in per-scene optimization.

Building on this representation, we address the generative modeling task using the latent diffusion paradigm. We encode 3D assets into a set of latent tokens and model their distribution. However, we identify a critical challenge in applying diffusion to unordered set-structured latents [Li et al. 2025c; Zhang et al. 2023, 2024c]: the permutation ambiguity leads to conflicting gradient signals that can significantly slow convergence and degrade generation quality. To resolve this, we propose *VecSeq*, a canonical re-indexing strategy. We map the unordered latent tokens to a deterministic, low-discrepancy 3D Sobol sequence using optimal transport [Berger et al. 2009]. This imposes a stable spatial ordering on the latents, transforming the

difficult set-generation problem into a robust sequence-generation task.

Our contributions are summarized as follows:

- We introduce Density-Sampled Gaussians (DeG), a 3D representation designed for generative modeling that supports variable-sized outputs and adaptive allocation of Gaussians by sampling centers from a learnable density function.
- We derive the *render loss contribution gradient*, an efficient signal that enables end-to-end optimization of the stochastic density function using only image reconstruction loss, effectively learning optimal primitive placement.
- We propose *VecSeq*, a latent re-indexing mechanism that stabilizes diffusion training on point sets by anchoring tokens to a deterministic spatial structure, achieving faster convergence and state-of-the-art generation quality.

2 Related Work

2.1 3D Gaussian Splatting

3D Gaussian Splatting (3DGS) [Kerbl et al. 2023; Yu et al. 2024] represents a scene or object as a set of anisotropic Gaussians. Rendering is performed via differentiable rasterization, commonly referred to as splatting, which achieves real-time speed and high visual quality. As a result, 3DGS has recently become popular for photorealistic rendering. Recent improvements to 3DGS include enhanced densification [Rota Bulò et al. 2024; Ye et al. 2024], efficient training [Kheradmand et al. 2024; Lan et al. 2025; Mallick et al. 2024], sparse-view reconstruction [Li et al. 2024; Xiong et al. 2023], and instant feed-forward inference [Tang et al. 2024a; Xu et al. 2024; Zhang et al. 2024a; Ziwen et al. 2025]. F4Splat [Kim et al. 2026] extends densification to feed-forward reconstruction by learning heuristic densification scores. These works aim for reconstruction and generally lack the ability to generate 3D Gaussians.

2.2 3D Generative Models

Early 3D generation methods focused on explicit 3D representations (e.g., voxels, point clouds, and meshes) and used adversarial training to model category-level shape distributions [Gao et al. 2022; Wu et al. 2016]. With the advent of large-scale 2D diffusion priors, score distillation sampling (SDS) enables 3D generation by optimizing through gradients distilled from a frozen diffusion model, without requiring curated 3D training data [Poole et al. 2022]. Subsequent works improve the efficiency and realism of SDS-based optimization by refining gradient formulations [Wang et al. 2023; Yan et al. 2025], introducing additional priors [Chen et al. 2023; Long et al. 2024; Qiu et al. 2024], and accelerating convergence [Liang et al. 2024; Tang et al. 2024b]. Despite these advances, optimization-based pipelines remain computationally expensive, motivating feed-forward large reconstruction models [Hong et al. 2023] that amortize reconstruction by training scalable transformers on large-scale multi-view data, enabling 3D asset prediction from images [Liu et al. 2023b,a; Shi et al. 2023; Wu et al. 2024b; Xu et al. 2024].

More recently, the success of latent diffusion models (LDMs) [Romach et al. 2022] has inspired 3D-native latent representations for

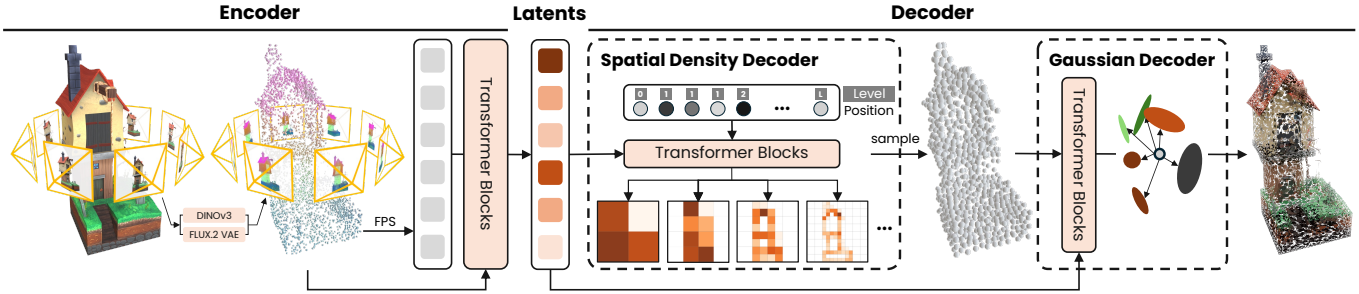


Fig. 2. Overview of the DeG-VAE. Multi-view renderings are encoded using off-the-shelf feature extractors, and the features are projected to randomly sampled surface points. Points with features are encoded into latent tokens following 3DShape2VecSet [Zhang et al. 2023]. Taking the latent tokens as the condition, a spatial density decoder models the spatial distribution of Gaussians, and a Gaussian decoder predicts Gaussian attributes for differentiable rendering. Note that the rendering loss can be back-propagated to the spatial density decoder, allowing for adaptive density control.

scalable 3D generation. 3DShape2VecSet [Zhang et al. 2023] proposes a paradigm that encodes signed distance fields into an unordered set of latent tokens and performs diffusion in this latent space. More generally, unordered set generation has been explored for 3D point sets [Fan et al. 2017]. CLAY [Zhang et al. 2024c] further develops this direction with scaled-up data processing and training, achieving large-scale asset generation. Notable follow-ups along this line include TripoSG [Li et al. 2025c], Hunyuan 2.1 [Hunyuan3D et al. 2025], and Direct3D [Wu et al. 2024a], among others. While LATTICE [Lai et al. 2025] further extends the set generation paradigm with a two-stage coarse-to-fine pipeline. Another branch of latent 3D generation seeks to improve geometric detail via sparse voxel hierarchies [Ren et al. 2024] or sparse structures [Li et al. 2025a; Wu et al. 2025; Xiang et al. 2025b]. These works primarily target surface geometry generation, and relatively few focus on generating 3D Gaussians.

2.3 Generation of 3D Gaussians

We focus on generating high-quality 3D Gaussians. Simply combining Gaussian representations with optimization-based pipelines (e.g., DreamGaussian [Tang et al. 2024b]) is often insufficient, as performance is bounded by the 2D vision priors and the optimization remains costly. Recent works explore feed-forward generation to improve efficiency, while existing approaches are typically constrained by their neural output parameterization. Structured-latent methods [Wu et al. 2025; Xiang et al. 2025b] assign a fixed number of Gaussians to each voxel in a sparse 3D structure. Pixel-aligned lifting approaches [Tang et al. 2024a; Xu et al. 2024; Zhang et al. 2024a], inspired by LRM- or VGGT-style pipelines [Wang et al. 2025], predict a fixed number of Gaussians per pixel or patch. Due to these architectural constraints, such methods struggle to preserve the key advantage of 3D Gaussians: a highly flexible representation that can adaptively allocate capacity to important regions. GaussianCube [Zhang et al. 2024b] attempts to recover output flexibility by constructing an optimal-transport mapping between structured grids and a target set of Gaussians, where the targets are obtained by per-object Gaussian fitting. This introduces substantial training overhead: generating ground-truth Gaussians via per-object fitting is time-consuming, and the method still typically produces

a fixed number of Gaussians due to the underlying grid resolution. AtlasGaussian [Yang et al. 2024] represents 3D Gaussians by sampling from learned UV patches. While it can generate arbitrarily many primitives in principle, it samples uniformly within each patch, which does not model a global adaptive distribution and limits representational flexibility. MaskGaussian [Liu et al. 2025] treats Gaussians as probabilistic entities via predicted masks, but still operates on a fixed spatial scaffold without learning a global density.

3 Method

3.1 Overview

Our pipeline aims to bridge the gap between fixed-structure generative models and the adaptive nature of 3DGS. While we follow the latent diffusion paradigm [Rombach et al. 2022], we diverge from approaches that constrain Gaussians to regular fixed-size structures [Xiang et al. 2025b; Zhang et al. 2024b]. Instead, we introduce a representation that naturally supports variable resolution and adaptive allocation. Our method consists of two core components: (1) A *Density-sampled Gaussian VAE (DeG-VAE)*, which encodes 3D assets into a compact latent space and decodes them via a learned spatial probability density. This allows the model to allocate Gaussian primitives dynamically and to train the VAE end-to-end with a novel density-aware multi-view rendering loss (Sec. 3.2 and Sec. 3.3). (2) A *VecSeq* diffusion transformer, which models the distribution of these latent tokens and is trained to recover the latents conditioned on a single input image. To address the convergence challenge of diffusion on unordered sets, VecSeq introduces a canonical re-indexing mechanism based on optimal transport, enabling robust and scalable generation (Sec. 3.4). Figure 2 provides a high-level overview of the pipeline, while Figure 4 illustrates the detailed neural architectures of these components. We detail each component in the following subsections.

3.2 Density-sampled Gaussian VAE

The core of our representation is the decoupling of *geometric distribution* (i.e., where primitives exist) from *primitive attributes* (i.e., appearance and local shape).

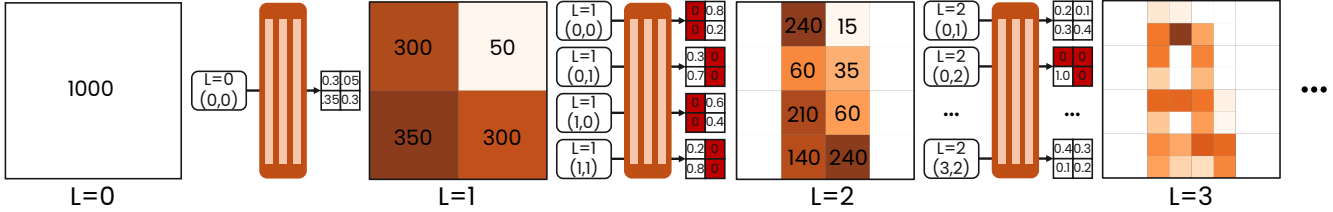


Fig. 3. A 2D illustration of the point sampling process. Starting from the coarsest level, the network iteratively predicts the density value for each occupied voxel at the current level until the finest level is reached. Integers in the grid denote the number of points allocated to each voxel, given a target of 1,000 points for point sampling.

Set Encoder. For a 3D asset \mathcal{O} , we represent its geometry and appearance as a set of latent tokens $\mathcal{Z} = \{z_i \in \mathbb{R}^{C_i}\}_{i=1}^M$, adhering to the set-latent paradigm [Zhang et al. 2023]. To capture high-fidelity details, we aggregate information from both multi-view RGB renderings and explicit surface geometry. We render K views of \mathcal{O} given camera poses $\{\pi_k\}_{k=1}^K$ and extract feature maps using DINOv3 [Siméoni et al. 2025] for semantic consistency and a FLUX.2 VAE [Labs 2025] for high-frequency texture details. Simultaneously, we sample a dense point cloud $\mathcal{P} = \{p_i\}_{i=1}^{N_1}$ from the asset surface. Following TRELIS [Xiang et al. 2025b], we project each point p_i onto the multi-view feature maps and average the retrieved features across all views (occlusions are not handled, following prior work [Xiang et al. 2025b]). This yields two complementary feature-augmented point sets:

$$\mathcal{P}^{\text{dinov3}} = \{f_i \in \mathbb{R}^{C_1}, p_i \in \mathbb{R}^3\}_{i=1}^{N_1}, \quad (1)$$

$$\mathcal{P}^{\text{flux2}} = \{f_i \in \mathbb{R}^{C_2}, p_i \in \mathbb{R}^3\}_{i=1}^{N_2}, \quad (2)$$

We compress these variable-length point features into a fixed-size latent set \mathcal{Z} using a transformer-based set encoder \mathcal{E}_θ :

$$\mathcal{Z} = \mathcal{E}_\theta(\text{FPS}(\mathcal{P}) | \mathcal{P}^{\text{dinov3}}, \mathcal{P}^{\text{flux2}}), \quad (3)$$

where FPS denotes Farthest Point Sampling, selecting M representative centers to seed the encoder attention.

Stochastic Density Decoding. Standard 3D decoders typically map latent tokens to a fixed number of primitives or a uniform voxel grid. This ignores a fundamental property of 3DGS: visual quality depends on the *adaptive* concentration of primitives in regions of high geometric or textural complexity [Kerbl et al. 2023; Mallick et al. 2024; Ren et al. 2025]. To bake this adaptivity into the generative model, we formulate Gaussian center prediction as a sampling process from a learned conditional probability density $q_\theta(x | \mathcal{Z})$ over \mathbb{R}^3 . At inference time, we draw P *anchor points* from this density:

$$\mathcal{P}_{\text{anchor}} = \{x_i\}_{i=1}^P \sim q_\theta(\cdot | \mathcal{Z}). \quad (4)$$

Crucially, P is not fixed by the architecture; it can be adjusted at inference time to trade off rendering speed for fidelity.

Efficient Octree-Based Sampling. Defining q_θ over a dense voxel grid is computationally prohibitive ($O(N^3)$). Instead, we parameterize the density using an L -level octree factorization, enabling an effective resolution of $(2^L)^3$ while maintaining sparse computation.

Let $x_{0:l}$ denote the index of an octree cell at level l along the path to x . We factorize the joint probability as:

$$q_\theta(x | \mathcal{Z}) = \prod_{l=1}^L q_\theta(x_{0:l} | x_{0:l-1}, \mathcal{Z}), \quad (5)$$

where each term represents an 8-way categorical distribution over the children of a parent cell. Each conditional $q_\theta(x_{0:l} | x_{0:l-1}, \mathcal{Z})$ is implemented as a shared transformer θ that cross-attends to the latent tokens \mathcal{Z} and outputs 8 logits for the active parent cell. We implement this via efficient ancestral sampling (details in Supplementary). We maintain a frontier of *active cells* containing samples. At each level, we only evaluate the probability logits for active cells, routing samples to children based on q_θ . Empty branches are naturally pruned, and the process repeats until level L . This yields discrete leaf indices, which are dequantized into continuous anchor positions $\mathcal{P}_{\text{anchor}}$ via uniform sampling within the leaf volume. A 2D illustration of the sampling process is shown in Fig. 3.

Attribute Decoding and Local Expansion. With the sampled anchors $\mathcal{P}_{\text{anchor}}$ establishing the spatial support of the representation, the renderable geometry and appearance are resolved in a subsequent stage. Given the anchors and global latents \mathcal{Z} , we employ a transformer-based attribute decoder to predict the parameters of the Gaussian primitives (opacity, scaling, rotation, and spherical harmonic coefficients). To further capture local surface details, we implement a local expansion mechanism: each anchor x_i spawns K individual Gaussians with learned local offsets:

$$\{\{g_i^k\}_{k=1}^K\}_{i=1}^P = \mathcal{D}_\theta(\mathcal{P}_{\text{anchor}} | \mathcal{Z}), \quad (6)$$

where \mathcal{D}_θ is a learnable transformer-based attribute decoder, and the Gaussian position x_i^k is predicted by adding an offset to the anchor x_i . This hierarchical approach, i.e., global density sampling followed by local expansion, allows the model to represent large uniform areas with few anchors while densely populating complex details, yielding $N = P \cdot K$ total splats.

3.3 Differentiable Density Optimization

A key challenge in our pipeline is optimizing the spatial density q_θ . Standard methods rely solely on structural supervision (e.g., cross-entropy against surface voxels), which often misaligns with rendering needs: allocating too many primitives to flat, textured surfaces and too few to thin geometric structures. Ideally, we want to update the density based on *rendering* feedback. However, because

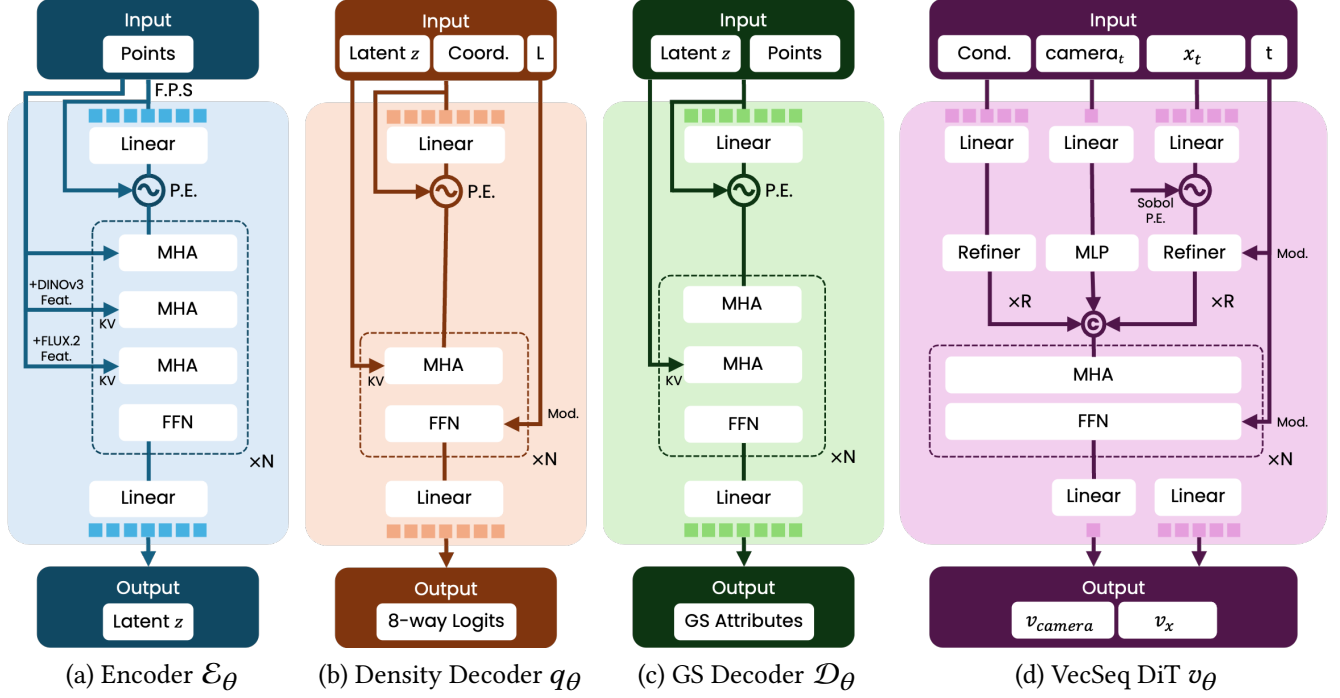


Fig. 4. Detailed architecture for encoding, decoding, and generation. The refiners in (d) are transformer layers used for processing inputs from different modalities following S3-DiT [Cai et al. 2025a]. To enable RoPE [Su et al. 2024] for multi-modal input in the DiT, we use a lightweight head to predict the 3D index given the latent in each DiT layer, following RePo [Li et al. 2025b].

anchor locations $\mathcal{P}_{\text{anchor}}$ are samples from q_θ , the rendering loss $\mathcal{L}_{\text{render}}$ is not directly differentiable with respect to the density parameters θ . To bridge this gap, we derive the *render loss contribution gradient* that backpropagates rendering feedback into the probabilistic density, effectively performing “differentiable densification and pruning.”

Structural Initialization. We first anchor the density using explicit geometry. Given the target distribution $p(x)$ derived from surface points, we minimize the cross-entropy loss over the octree structure:

$$\mathcal{L}_{\text{CE}} = - \sum_{x_{0:L}} p(x_{0:L}) \log q_\theta(x_{0:L} | \mathcal{Z}) \quad (7)$$

$$= - \sum_{x_{0:L}} p(x_{0:L}) \sum_{l=1}^L \log q_\theta(x_{0:l} | x_{0:l-1}, \mathcal{Z}) \quad (8)$$

$$= - \sum_{l=1}^L \sum_{x_{0:l}} p(x_{0:l}) \log q_\theta(x_{0:l} | x_{0:l-1}, \mathcal{Z}), \quad (9)$$

where $x_{0:L}$ denotes a level- L leaf cell, $p(x_{0:L})$ is the normalized histogram of surface points assigned to leaves, and $p(x_{0:l})$ denotes its marginal distribution over level- l cells.

Rendering Supervision. For appearance supervision, we sample camera poses π and minimize image reconstruction losses between $\mathcal{R}(\mathcal{G}, \pi)$ and the target images, where \mathcal{R} is the differentiable Gaussian splatting rendering function and \mathcal{G} is the set of decoded 3D Gaussian primitives. We minimize the weighted sum of L1 loss,

SSIM loss and LPIPS loss:

$$\mathcal{L}_{\text{render}} = \mathcal{L}_{\text{l1}} + \lambda_{\text{ssim}} \mathcal{L}_{\text{ssim}} + \lambda_{\text{lpiips}} \mathcal{L}_{\text{lpiips}}. \quad (10)$$

Backpropagating Rendering to Density. Unlike prior works [Xiang et al. 2025b] that treat structure and appearance as separate optimization problems, we unify them. We seek to minimize the expected rendering loss over the density distribution. Specifically, we also propagate rendering supervision to the structural density stochastic density decoder q_θ and regard the structural loss \mathcal{L}_{CE} mainly as a regularizer. The loss gradient with respect to anchors $\mathcal{P}_{\text{anchor}}$, which are sampled from the decoded densities, cannot be directly propagated to VAE parameters θ . Fortunately, we note that the gradient of the expectation of the rendering loss with respect to the density distribution can be computed:

$$\nabla_\theta \mathcal{L}_{\text{render}} = \nabla_\theta \mathbb{E}_{x_i \sim q_\theta} [\mathcal{L}_{\text{render}}(\mathcal{P}_{\text{anchor}} = \{x_i\}_{i=1}^P)] \quad (11)$$

$$= \mathbb{E} \left[\mathcal{L}(\{x_i\}_{i=1}^P) \nabla_\theta \log \left(\prod_{j=1}^P q_\theta(x_j) \right) \right] \quad (12)$$

$$= \mathbb{E} \left[\sum_{j=1}^P \mathcal{L}(\{x_i\}_{i=1}^P) \nabla_\theta \log(q_\theta(x_j)) \right] \quad (13)$$

$$= \mathbb{E} \left[\sum_{j=1}^P (\mathcal{L}(\{x_i\}_{i=1}^P) - \mathcal{L}(\{x_i\}_{i \neq j}^P)) \nabla_\theta \log(q_\theta(x_j)) \right], \quad (14)$$

where Eq. 13 corresponds to the standard policy-gradient [Sutton et al. 1999], and Eq. 14 can be interpreted as an advantage estimation, also known as difference reward [Tumer and Agogino 2007; Wolpert and Tumer 2001]. Here, $\{x_i\}_{i \neq j}^P$ denotes the anchor set excluding x_j . The difference term $\Delta \mathcal{L}_{\text{render}} = \mathcal{L}_{\text{render}}(\{x_i\}_{i=1}^P) - \mathcal{L}_{\text{render}}(\{x_i\}_{i \neq j}^P)$ measures how much anchor x_j decreases the rendering loss; Intuitively, this term increases the probability density at locations where the presence of anchor x_j leads to a larger reduction in rendering error.

Efficient render loss contribution gradient. Directly evaluating Eq. 14 remains impractical, since each leave-one-out baseline would require an additional rendering pass for every sampled anchor. Our key observation is that, for the pixel-wise \mathcal{L}_{11} term in $\mathcal{L}_{\text{render}}$, the standard 3DGS backward rasterization already maintains the transmittance and accumulated back color needed to estimate the loss change caused by removing a primitive. We therefore accumulate primitive-level contributions inside the same CUDA backward pass at negligible overhead, sum them over primitives from the same anchor, and directly backpropagate the resulting anchor-level signal to $\log(q_\theta(x_j | \mathcal{Z}))$. This fused computation relies on the additive per-pixel structure of \mathcal{L}_{11} ; full primitive-level derivations and CUDA implementation details are provided in the supplementary material. Finally, our VAE model is trained with a combination of structural supervision and rendering supervision via:

$$\mathcal{L}_{\text{VAE}} = \lambda_{\text{struct}} \mathcal{L}_{\text{CE}} + \lambda_{\text{render}} (\mathcal{L}_{\text{render}} + \hat{\mathcal{L}}_{\text{render}}) + \lambda_{\text{reg}} \mathcal{L}_{\text{reg}} + \lambda_{\text{kl}} \mathcal{L}_{\text{kl}}, \quad (15)$$

where $\hat{\mathcal{L}}_{\text{render}}$ denotes the additional render loss contribution gradient described above, and \mathcal{L}_{reg} is a regularization term on predicted GS parameters (details are provided in the Supplementary).

We optimize this objective using a three-stage curriculum.

Stage 1 (Structural Initialization): We optimize \mathcal{E}_θ and q_θ using only \mathcal{L}_{CE} to establish a coarse geometric hull, analogous to standard 3DGS initialization (e.g., SfM-derived). This prevents degenerate solutions (e.g., zero-opacity collapse) from random Gaussians, and takes only $\sim 6\%$ of total training time.

Stage 2 (Appearance): We train the attribute decoder \mathcal{D}_θ with a small gaussian count and large batch size using $\mathcal{L}_{\text{render}} + \mathcal{L}_{\text{CE}}$, locking in appearance. This accelerates convergence and is optional.

Stage 3 (Joint Refinement): We train all parameters end-to-end with the full \mathcal{L}_{VAE} , enabling $\hat{\mathcal{L}}_{\text{render}}$ to provide signals for density reallocation. We also randomize the number of anchors P to encourage the model to generalize across different resolution budgets.

3.4 VecSeq Diffusion

We model the distribution of latent codes \mathcal{Z} using a diffusion transformer. We adopt the Flow Matching framework [Lipman et al. 2022] with an S3-DiT backbone [Cai et al. 2025a]. The training objective is

$$\mathcal{L}_{\text{FM}} = \mathbb{E}_{t, x_0, \epsilon} \|v_\theta(x_t, t) - (\epsilon - x_0)\|_2^2, \quad (16)$$

where x_t is the latent state at time t , interpolated between data x_0 and noise ϵ . To recover the conditioning-view pose, we jointly

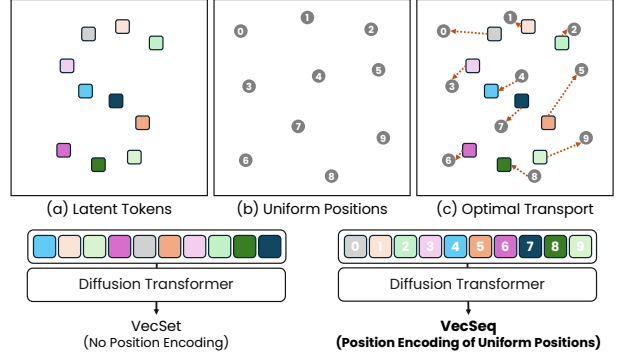


Fig. 5. VecSeq re-indexing. Latent tokens are associated with 3D positions during encoding and then canonically ordered by matching them to deterministic 3D Sobol anchors, turning an unordered latent set into a stable vector sequence for diffusion denoising.

predict a compact noisy camera token c_t and concatenate it to x_t during training. Details of c_t are provided in the supplementary material.

The Permutation Ambiguity. A fundamental challenge in training diffusion models on latent sets is permutation invariance. Our set encoder produces an unordered set of tokens $\mathcal{Z} = \{z_i\}_{i=1}^M$. Unlike pixels in an image, which have fixed coordinates, set tokens have no intrinsic ordering. If we feed these unordered sets directly to a diffusion model, the pairing between noise tokens and data tokens becomes arbitrary ($M!$ possible pairings). The model is forced to learn an average over all permutations, resulting in slow convergence and blurry, mode-averaged generations.

VecSeq: Canonical Serialization via Optimal Transport. To resolve this, we propose VecSeq, a method to transform the unordered latent set into a canonically ordered vector sequence. While the latent tokens z_i themselves lack coordinates, they are derived from surface points $p_i \in \text{FPS}(\mathcal{P})$ during encoding (Eq. 3). We could use these p_i to sort the tokens, but these positions are asset-specific and unknown at inference time.

Instead, we align the tokens to a *fixed, deterministic* spatial structure that is shared across all assets. We choose a 3D Sobol sequence [Sobol 1967] $\mathcal{S} = \{s_j\}_{j=1}^M$ as our anchor structure. Sobol sequences are low-discrepancy quasi-random sequences that cover the unit cube $[0, 1]^3$ more uniformly than standard random sampling, ensuring a balanced spatial scaffold. During training, we compute an optimal assignment π^* that matches the asset-specific FPS points $\{p_i\}$ to the fixed Sobol anchors $\{s_j\}$ by minimizing the total transport cost:

$$\pi^* = \text{3D OT Assign}(\{p_i\}, \{s_j\}). \quad (17)$$

We then reorder the latent tokens according to this map, yielding a sequence $\tilde{\mathcal{Z}} = \{\tilde{z}_j\}_{j=1}^M$ where $\tilde{z}_j = z_{\pi^*(j)}$. This assignment is computed once as an offline preprocessing step, incurring zero cost during training or inference.

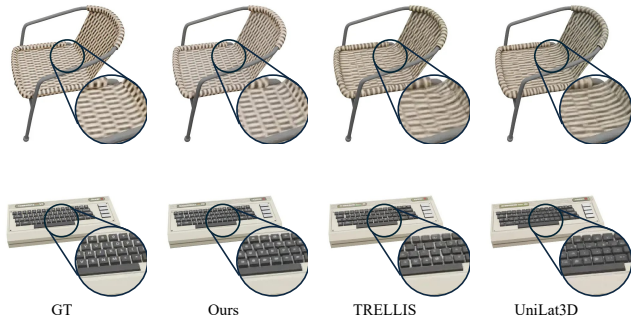


Fig. 6. Qualitative comparison of 3D reconstruction. Under a matched Gaussian budget (DeG-VAE with 262K vs. baselines with ≈ 310 K), our model achieves higher visual fidelity. As shown in the zoom-in views, DeG-VAE preserves fine details and complex structures significantly better than the baselines.

Crucially, this reordering associates the j -th token of *any* asset with the spatial region around the j -th Sobol anchor s_j . We inject this spatial prior into the diffusion model by adding a sinusoidal positional embedding of s_j to the j -th token. At inference time, the model simply predicts a sequence of length M , knowing implicitly that the j -th output corresponds to the spatial location s_j . This effectively converts the difficult set-generation problem into a stable sequence-generation problem, significantly improving convergence and fidelity.

Conceptually, this assignment is similar to GaussianCube [Zhang et al. 2024b], which also uses OT to assign Gaussians to a fixed cube structure; however, our assignment is performed over latent tokens rather than directly over Gaussian primitives. Moreover, using a single universal template, i.e., the Sobol anchors $\{s_j\}$, allows each object to be matched independently, yielding *linear* $O(N)$ complexity, unlike classical permutation synchronization methods [Huang and Guibas 2013] that require pairwise matching with $O(N^2)$ complexity and are intractable for large open-vocabulary datasets.

4 Experiments

We evaluate both the reconstruction component (DeG-VAE) and the generative component (latent diffusion on VecSeq). We report quantitative metrics and qualitative comparisons.

4.1 Implementation Details

We train DeG-VAE and the latent generation model on the Objaverse [Deitke et al. 2023b] and Objaverse-XL [Deitke et al. 2023a] subsets of the TRELLIS-500K dataset [Xiang et al. 2025b]. In the first stage of VAE training, we use 1024 latent tokens and use cross entropy loss to supervise 8192 points. In the second stage of VAE training, we randomly sample 1024 – 8192 tokens and 2048 anchors for GS rendering, corresponding to $N = 2048 \cdot K$ final Gaussians after local expansion. In the third stage of VAE training, we randomly sample 1024 – 8192 tokens and 1024 – 8192 anchors per asset for rendering (the two quantities are not necessarily identical). We train the VAE for approximately 10 days on 32 NVIDIA A800 GPUs and

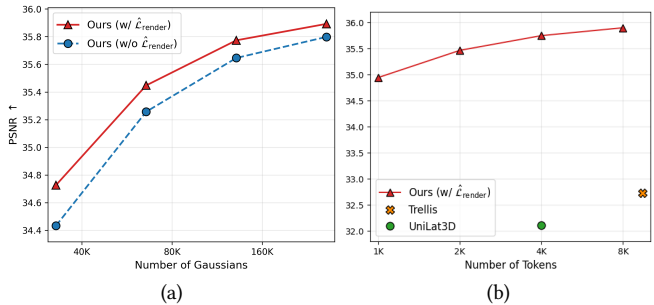


Fig. 7. Quantitative evaluation. PSNR versus (a) the number of decoded Gaussians and (b) the latent token length, comparing TRELLIS, UniLat3D, our method, and our method without the render loss contribution gradient ($\hat{\mathcal{L}}_{render}$).

the flow-matching model for approximately 11 days on 32 NVIDIA A800 GPUs.

For quantitative evaluation, we use the Toys4K dataset [Stojanov et al. 2021] for both reconstruction and generation; this test set is unseen during our model training. For qualitative results, we use a set of high-quality, self-collected images for image-conditioned generation.

4.2 Reconstruction Results

4.3 Generation Results

We evaluate the reconstruction performance of DeG-VAE on Toys4K. For each object, we render 16 viewpoints and compute image-level metrics between the ground-truth renderings and renderings from the decoded Gaussians. We report PSNR, SSIM, and LPIPS, and compare against representative baselines including TRELLIS [Xiang et al. 2025b] and UniLat3D [Wu et al. 2025]. As shown in Table 1 and Fig. 6, under a comparable Gaussian budget, DeG-VAE substantially outperforms all competitors across PSNR, SSIM, and LPIPS. TRELLIS and UniLat3D assign a fixed number of Gaussians to each voxel, which inevitably overspends capacity in simple regions while under-allocating it in complex ones. In contrast, DeG-VAE learns to allocate Gaussian density directly from rendering supervision, using the available Gaussians more effectively to maximize visual fidelity.

Variable-Sized Gaussians. A key advantage of the DeG representation is its ability to produce variable-sized Gaussian sets. This flexibility enables explicit trade-offs between rendering/memory cost and visual quality by varying the number of sampled anchors P , which determines the final Gaussian count $N = PK$ after local expansion. In Fig. 7 (a), we analyze reconstruction quality as a function of N . Performance improves steadily as the Gaussian count increases. Notably, DeG-VAE reaches the same visual quality (LPIPS) as TRELLIS while using less than 1/2 as many Gaussians.

Learned Density Control. To validate the effectiveness of optimizing density via rendering supervision with $\hat{\mathcal{L}}_{render}$, we train a Stage-3 VAE variant that disables $\hat{\mathcal{L}}_{render}$ while keeping all other settings and training steps fixed. Fig. 7 reports reconstruction quality



Fig. 8. Generation comparison. We compare our generated 3D Gaussian assets with representative textured 3D generation models under the same rendering settings. Our model can generate 3D Gaussians with accurate structure and appearance details.

Table 1. Quantitative reconstruction results on the Toys4K dataset. We compare our DeG-VAE against baselines in terms of PSNR \uparrow , SSIM \uparrow , and LPIPS \downarrow . Our method consistently outperforms competing approaches under a comparable Gaussian budget. Dec. records the decoding time per object on a single NVIDIA 4090 GPU (batch size=4).

Method	#Token(#Dim)	# Gaussians	Dec. (s)	PSNR \uparrow	SSIM \uparrow	LPIPS \downarrow
TRELIS	≈ 9679 ($\approx 77k$)	$\approx 310k$	0.034	32.72	0.9734	0.0269
UniLat3D	4096 ($32k$)	$\approx 310k$	0.074	32.10	0.9715	0.0307
Ours	8192 ($131k$)	262k	0.10	35.89	0.9787	0.0223

with and without $\hat{\mathcal{L}}_{\text{render}}$ across different decoded Gaussian counts. Incorporating $\hat{\mathcal{L}}_{\text{render}}$ consistently improves reconstruction, with the largest gains appearing in the low-budget regime, consistent with the intuition that adaptive allocation is most valuable when capacity is limited. We provide qualitative visualizations of this effect, including comparisons of the generated anchor point clouds, in the supplementary material.

Token Length. Latent token length controls the degree of compression in our representation. In Fig. 7 (b), we visualize reconstruction quality as a function of token length and observe consistent improvements as more tokens are used, highlighting the favorable scaling behavior of DeG.

Quantitative comparison. We measure Gaussian generation performance using image-condition alignment (CLIP-I) and distributional metrics computed on rendered multi-view images (FD $_{\text{incep}}$,

KD $_{\text{incep}}$, FD $_{\text{dino}v2}$, and KD $_{\text{dino}v2}$). We detail the computation of these scores in the supplementary material. We compare against representative baselines, including mesh generation models (Hunyuan3D 2.1 [Hunyuan3D et al. 2025], TRELIS-2 [Xiang et al. 2025a]) and Gaussian generation models (GaussianAnything [Lan et al. 2024], LGM [Tang et al. 2024a], DiffusionGS [Cai et al. 2025b], TRELIS [Xiang et al. 2025b], UniLat3D [Wu et al. 2025]). Table 2 shows that our method achieves the highest image-conditioning alignment score and delivers the best performance on most distributional metrics, demonstrating state-of-the-art 3D generation with strong visual consistency.

Qualitative comparison. We present qualitative comparisons in Fig. 15. Our method excels in both generation quality and image-prompt alignment compared with prior approaches, producing higher-fidelity 3D Gaussian results with more detailed geometry

Table 2. 3DGS generation metrics. CLIP-I measures image-level cosine similarity between rendered and prompt images. We report FD_{\downarrow} , KD_{\downarrow} , and $CLIP-I_{\uparrow}$ on rendered multi-view images. The best results are shown in bold, and the second-best results are underlined.

Method	Repr.	CLIP-I \uparrow	$FD_{\text{incep}} \downarrow$	$KD_{\text{incep}} \downarrow$	$FD_{\text{dinov2}} \downarrow$	$KD_{\text{dinov2}} \downarrow$
Hunyuan3D 2.1	Mesh	89.09	4.86	<u>0.05</u>	95.55	7.99
TRELLIS-2	Mesh	89.83	4.55	<u>0.05</u>	63.36	2.74
LGM	3DGS	80.49	35.7	1.74	626.4	112.4
DiffusionGS	3DGS	84.82	15.7	0.49	287.9	34.52
TRELLIS	3DGS	91.68	<u>2.55</u>	0.02	<u>33.39</u>	1.3
UniLat3D	3DGS	<u>91.69</u>	2.72	0.02	33.71	1.3
Ours	3DGS	92.26	2.42	0.02	31.16	<u>1.4</u>

Table 3. Reordering ablation. Both variants use the same encoder and decoder weights trained with VecSet-style unordered latents; the only difference is whether Sobol-anchor positional embeddings (PE) are added to the reordered tokens in diffusion training. The diffusion model is trained for the same number of steps (80K). $KD_{\text{dinov2}} \downarrow$ is reported $100\times$.

	CLIP-I \uparrow	$FD_{\text{dinov2}} \downarrow$	$KD_{\text{dinov2}} \downarrow$
w/o reordering (VecSet)	89.39	75.08	4.79
w/ reordering (Ours)	90.01	66.94	3.81

and texture. In addition, our generations better match prompt colors and preserve fine-grained details in the corresponding object parts.

Effect of Token Reordering (VecSeq vs. VecSet). We compare VecSeq against a VecSet-style baseline that uses the same encoder and decoder weights and differs only in whether VecSeq reordering is applied during diffusion training. Without reordering, the Sobol-anchor positional embeddings carry no consistent spatial meaning; the same index can correspond to different geometric features across objects, effectively reducing the model to a VecSet-style baseline. In contrast, VecSeq reordering via OT makes each token index consistently correspond to the same spatial region, allowing the positional encoding to become informative. Table 3 shows that reordering improves both prompt alignment and distributional quality.

5 Conclusions

In this work, we presented Density-Sampled Gaussians (DeG), a generative 3D Gaussian representation that replaces non-differentiable densification and pruning with a learnable, rendering-optimized density defined over an octree. By sampling Gaussian centers from this density, DeG supports variable-sized outputs and adaptive allocation of Gaussians to locally complex regions, enabling favorable trade-offs between fidelity and rendering cost. We further introduced a paired learning pipeline that trains an autoencoder to compress 3D assets into compact latent tokens and decode them into DeG, with density optimized end-to-end under rendering supervision. Our experiments demonstrate that this design translates into substantially improved reconstruction quality under a comparable Gaussian budget $N = PK$, and that the render loss contribution gradient($\mathcal{L}_{\text{render}}$)

provides consistent gains, especially in low-budget regimes where smart allocation matters most. DeG also exhibits strong scaling behavior: reconstruction improves smoothly as either the sampled anchor count P (and therefore the final Gaussian count N) or the latent token length increases. Finally, we addressed a key convergence challenge in generative modeling with vector-set latents arising from permutation ambiguity in diffusion training. Our proposed VecSeq formulation assigns token positions via optimal transport to enable positional encoding, leading to faster convergence and higher-quality single-image conditional generation. Together, these contributions establish a practical and scalable foundation for high-fidelity 3D Gaussian generation and open new opportunities for controllable, resource-aware 3D content synthesis.

Limitations and Future Work. Despite these strengths, DeG has several limitations. First, as a single-image-to-3D method, back-facing regions are not observed during inference and may exhibit lower quality; failure-case visualizations and analysis are provided in the supplementary material. Second, our representation currently only targets 3DGS rather than meshes; however, because the latent space faithfully reconstructs both 3D shape and texture, it might already contain the necessary information for a textured mesh decoder, making direct textured mesh generation a promising direction for future work.

Acknowledgments

This work was supported in part by the International (Hong Kong, Macao, and Taiwan) Collaborative R&D Project, Beijing Major Science and Technology Project under Contract No.Z251100007125016.

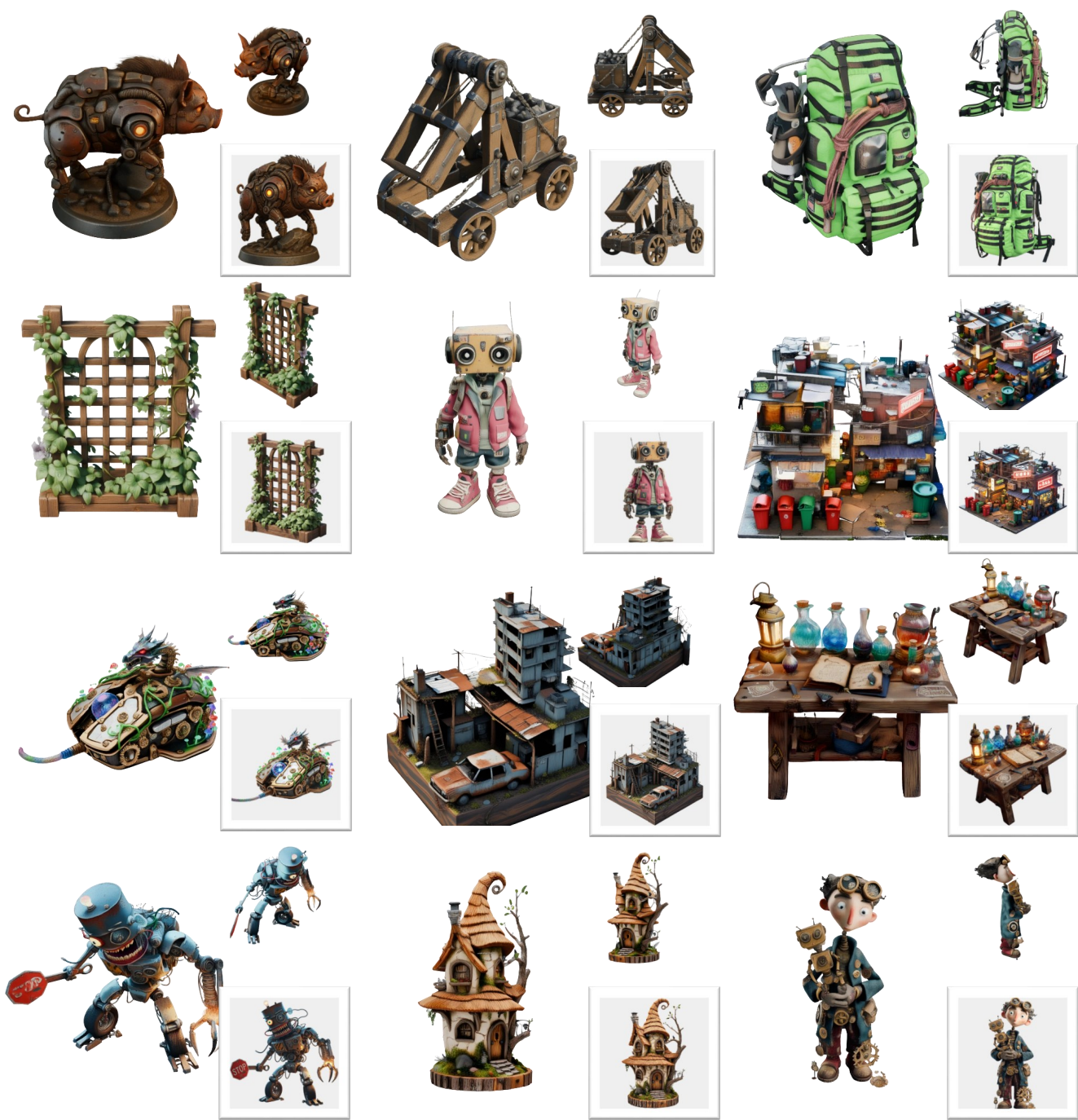


Fig. 9. Generated samples. A full-page gallery of diverse 3D Gaussian generations from our model, rendered from two different viewpoints.

References

- M Berger, B Eckmann, P Harpe, F Hirzebruch, N Hitchin, L Hörmander, A Kupiainen, G Lebeau, M Ratner, D Serre, et al. 2009. *Optimal transport: Old and new*. Springer.
- Huanqia Cai, Sihan Cao, Ruoyi Du, Peng Gao, Steven Hoi, Zhaohui Hou, Shijie Huang, Dengyang Jiang, Xin Jin, Liangchen Li, et al. 2025a. Z-Image: An Efficient Image Generation Foundation Model with Single-Stream Diffusion Transformer. *arXiv preprint arXiv:2511.22699* (2025).
- Yuanhao Cai, He Zhang, Kai Zhang, Yixun Liang, Mengwei Ren, Fujun Luan, Qing Liu, Soo Ye Kim, Jianming Zhang, Zhifei Zhang, et al. 2025b. Baking gaussian splatting into diffusion denoiser for fast and scalable single-stage image-to-3d generation and reconstruction. In *Proceedings of the IEEE/CVF International Conference on Computer Vision*. 25062–25072.
- Rui Chen, Yongwei Chen, Ningxin Jiao, and Kui Jia. 2023. Fantasia3d: Disentangling geometry and appearance for high-quality text-to-3d content creation. In *Proceedings of the IEEE/CVF international conference on computer vision*. 22246–22256.
- Matt Deitke, Ruoshi Liu, Matthew Wallingford, Huong Ngo, Oscar Michel, Aditya Kusupati, Alan Fan, Christian Laforte, Vikram Voleti, Samir Yitzhak Gadre, et al. 2023a. Objaverse-xl: A universe of 10m+ 3d objects. *Advances in Neural Information Processing Systems* 36 (2023), 35799–35813.
- Matt Deitke, Dustin Schwenk, Jordi Salvador, Luca Weihs, Oscar Michel, Eli VanderBilt, Ludwig Schmidt, Kiana Ehsani, Aniruddha Kembhavi, and Ali Farhadi. 2023b. Objaverse: A universe of annotated 3d objects. In *Proceedings of the IEEE/CVF conference on computer vision and pattern recognition*. 13142–13153.
- Haoqiang Fan, Hao Su, and Leonidas J Guibas. 2017. A point set generation network for 3d object reconstruction from a single image. In *Proceedings of the IEEE conference on computer vision and pattern recognition*. 605–613.
- Jun Gao, Tianchang Shen, Zian Wang, Wenzheng Chen, Kangxue Yin, Daiqing Li, Or Litany, Zan Gojic, and Sanja Fidler. 2022. Get3d: A generative model of high quality 3d textured shapes learned from images. *Advances in neural information processing systems* 35 (2022), 31841–31854.
- Alex Hanson, Allen Tu, Vasu Singla, Mayuka Jayawardhana, Matthias Zwicker, and Tom Goldstein. 2025. Pup 3d-gs: Principled uncertainty pruning for 3d gaussian splatting. In *Proceedings of the Computer Vision and Pattern Recognition Conference*. 5949–5958.
- Yicong Hong, Kai Zhang, Jiuxiang Gu, Sai Bi, Yang Zhou, Difan Liu, Feng Liu, Kalyan Sunkavalli, Trung Bui, and Hao Tan. 2023. Lrm: Large reconstruction model for single image to 3d. *arXiv preprint arXiv:2311.04400* (2023).
- Qi-Xing Huang and Leonidas Guibas. 2013. Consistent shape maps via semidefinite programming. In *Computer graphics forum*, Vol. 32. Wiley Online Library, 177–186.
- Team Hunyuan3D, Shuhui Yang, Mingxin Yang, Yifei Feng, Xin Huang, Sheng Zhang, Zebin He, Di Luo, Haolin Liu, Yunfei Zhao, et al. 2025. Hunyuan3D 2.1: From Images to High-Fidelity 3D Assets with Production-Ready PBR Material. *arXiv preprint arXiv:2506.15442* (2025).
- Bernhard Kerbl, Georgios Kopanas, Thomas Leimkühler, and George Drettakis. 2023. 3D Gaussian splatting for real-time radiance field rendering. *ACM Trans. Graph.* 42, 4 (2023), 139–1.
- Shakiba Kheradmand, Daniel Rebain, Gopal Sharma, Weiwei Sun, Yang-Che Tseng, Hossam Isack, Abhishek Kar, Andrea Tagliasacchi, and Kwang Moo Yi. 2024. 3d gaussian splatting as markov chain monte carlo. *Advances in Neural Information Processing Systems* 37 (2024), 80965–80986.
- Injae Kim, Chaehyeon Kim, Minseong Bae, Minseok Joo, and Hyunwoo J Kim. 2026. F4Splat: Feed-Forward Predictive Denoification for Feed-Forward 3D Gaussian Splatting. *arXiv preprint arXiv:2603.21304* (2026).
- Black Forest Labs. 2025. FLUX.2: Frontier Visual Intelligence. <https://bfl.ai/blog/flux-2>.
- Zejiang Lai, Yunfei Zhao, Zibo Zhao, Haolin Liu, Qingxiang Lin, Jingwei Huang, Chunchao Guo, and Xiangyu Yue. 2025. LATTICE: Democratize High-Fidelity 3D Generation at Scale. *arXiv preprint arXiv:2512.03052* (2025).
- Lei Lan, Tianjia Shao, Zixuan Lu, Yu Zhang, Chenfanfu Jiang, and Yin Yang. 2025. 3dgs2: Near second-order converging 3d gaussian splatting. In *Proceedings of the Special Interest Group on Computer Graphics and Interactive Techniques Conference Papers*. 1–10.
- Yushi Lan, Shangchen Zhou, Zhaoyang Lyu, Fangzhou Hong, Shuai Yang, Bo Dai, Xingang Pan, and Chen Change Loy. 2024. GaussianAnything: Interactive Point Cloud Flow Matching For 3D Object Generation. *arXiv preprint arXiv:2411.08033* (2024).
- Huayang Li, Tianyu Zhao, Deng Cai, and Richard Sproat. 2025b. RePo: Language Models with Context Re-Positioning. *arXiv preprint arXiv:2512.14391* (2025).
- Jiahe Li, Jiawei Zhang, Xiao Bai, Jin Zheng, Xin Ning, Jun Zhou, and Lin Gu. 2024. Dngaussian: Optimizing sparse-view 3d gaussian radiance fields with global-local depth normalization. In *Proceedings of the IEEE/CVF conference on computer vision and pattern recognition*. 20775–20785.
- Yanguang Li, Zi-Xin Zou, Zexiang Liu, Dehu Wang, Yuan Liang, Zhipeng Yu, Xingchao Liu, Yuan-Chen Guo, Ding Liang, Wanli Ouyang, et al. 2025c. TripoSG: High-Fidelity 3D Shape Synthesis using Large-Scale Rectified Flow Models. *arXiv preprint arXiv:2502.06608* (2025).
- Zhihao Li, Yufei Wang, Heliang Zheng, Yihao Luo, and Bihan Wen. 2025a. Sparc3D: Sparse Representation and Construction for High-Resolution 3D Shapes Modeling. *arXiv preprint arXiv:2505.14521* (2025).
- Yixun Liang, Xin Yang, Jiantao Lin, Haodong Li, Xiaogang Xu, and Yingcong Chen. 2024. Luciddreamer: Towards high-fidelity text-to-3d generation via interval score matching. In *Proceedings of the IEEE/CVF conference on computer vision and pattern recognition*. 6517–6526.
- Yaron Lipman, Ricky TQ Chen, Heli Ben-Hamu, Maximilian Nickel, and Matt Le. 2022. Flow matching for generative modeling. *arXiv preprint arXiv:2210.02747* (2022).
- Minghua Liu, Chao Xu, Haian Jin, Linghao Chen, Mukund Varma T, Zexiang Xu, and Hao Su. 2023b. One-2-3-45: Any single image to 3d mesh in 45 seconds without per-shape optimization. *Advances in Neural Information Processing Systems* 36 (2023), 22226–22246.
- Ruoshi Liu, Rundi Wu, Basile Van Hoorick, Pavel Tokmakov, Sergey Zakharov, and Carl Vondrick. 2023a. Zero-1-to-3: Zero-shot one image to 3d object. In *Proceedings of the IEEE/CVF international conference on computer vision*. 9298–9309.
- Yifei Liu, Zhihang Zhong, Yifan Zhan, Sheng Xu, and Xiao Sun. 2025. Maskgaussian: Adaptive 3d gaussian representation from probabilistic masks. In *Proceedings of the Computer Vision and Pattern Recognition Conference*. 681–690.
- Xiaoxiao Long, Yuan-Chen Guo, Cheng Lin, Yuan Liu, Zhiyang Dou, Lingjie Liu, Yuexin Ma, Song-Hai Zhang, Marc Habermann, Christian Theobalt, et al. 2024. Wonder3d: Single image to 3d using cross-domain diffusion. In *Proceedings of the IEEE/CVF conference on computer vision and pattern recognition*. 9970–9980.
- Saswat Subhajiyo Mallick, Rahul Goel, Bernhard Kerbl, Markus Steinberger, Francisco Vicente Carrasco, and Fernando De La Torre. 2024. Taming 3dgs: High-quality radiance fields with limited resources. In *SIGGRAPH Asia 2024 Conference Papers*. 1–11.
- Maxime Oquab, Timothée Darcet, Théo Moutakanni, Huy Vo, Marc Szafraniec, Vasil Khalidov, Pierre Fernandez, Daniel Haziza, Francisco Massa, Alaaeldin El-Nouby, et al. 2023. Dinov2: Learning robust visual features without supervision. *arXiv preprint arXiv:2304.07193* (2023).
- Ben Poole, Ajay Jain, Jonathan T Barron, and Ben Mildenhall. 2022. Dreamfusion: Text-to-3d using 2d diffusion. *arXiv preprint arXiv:2209.14988* (2022).
- Lingteng Qiu, Guanying Chen, Xiaodong Gu, Qi Zuo, Mutian Xu, Yushuang Wu, Weihao Yuan, Zilong Dong, Liefeng Bo, and Xiaoguang Han. 2024. Rindreamer: A generalizable normal-depth diffusion model for detail richness in text-to-3d. In *Proceedings of the IEEE/CVF conference on computer vision and pattern recognition*. 9914–9925.
- Alec Radford, Jong Wook Kim, Chris Hallacy, Aditya Ramesh, Gabriel Goh, Sandhini Agarwal, Girish Sastry, Amanda Askell, Pamela Mishkin, Jack Clark, et al. 2021. Learning transferable visual models from natural language supervision. In *International conference on machine learning*. PmlR, 8748–8763.
- Shiwei Ren, Tianci Wen, Yongchun Fang, and Biao Lu. 2025. FastGS: Training 3D Gaussian Splatting in 100 Seconds. *arXiv preprint arXiv:2511.04283* (2025).
- Xuanchi Ren, Jiahui Huang, Xiaohui Zeng, Ken Museth, Sanja Fidler, and Francis Williams. 2024. Xcube: Large-scale 3d generative modeling using sparse voxel hierarchies. In *Proceedings of the IEEE/CVF conference on computer vision and pattern recognition*. 4209–4219.
- Robin Rombach, Andreas Blattmann, Dominik Lorenz, Patrick Esser, and Björn Ommer. 2022. High-resolution image synthesis with latent diffusion models. In *Proceedings of the IEEE/CVF conference on computer vision and pattern recognition*. 10684–10695.
- Samuel Rota Bulò, Lorenzo Porzi, and Peter Kontschieder. 2024. Revisiting densification in gaussian splatting. In *European Conference on Computer Vision*. Springer, 347–362.
- Ruoxi Shi, Hansheng Chen, Zhuoyang Zhang, Minghua Liu, Chao Xu, Xinyue Wei, Linghao Chen, Chong Zeng, and Hao Su. 2023. Zero123++: a single image to consistent multi-view diffusion base model. *arXiv preprint arXiv:2310.15110* (2023).
- Oriane Siméoni, Huy V Vo, Maximilian Seitzer, Federico Baldassarre, Maxime Oquab, Cijo Jose, Vasil Khalidov, Marc Szafraniec, Seungeun Yi, Michaël Ramamonjisoa, et al. 2025. Dinov3. *arXiv preprint arXiv:2508.10104* (2025).
- Ilya M Sobol. 1967. Distribution of points in a cube and approximate evaluation of integrals. *USSR Computational mathematics and mathematical physics* 7 (1967), 86–112.
- Stefan Stojanov, Anh Thai, and James M Rehg. 2021. Using shape to categorize: Low-shot learning with an explicit shape bias. In *Proceedings of the IEEE/CVF conference on computer vision and pattern recognition*. 1798–1808.
- Jianlin Su, Murtadha Ahmed, Yu Lu, Shengfeng Pan, Wen Bo, and Yunfeng Liu. 2024. Roformer: Enhanced transformer with rotary position embedding. *Neurocomputing* 568 (2024), 127063.
- Richard S Sutton, David A McAllester, Satinder P. Singh, and Yishay Mansour. 1999. Policy Gradient Methods for Reinforcement Learning with Function Approximation. In *Advances in Neural Information Processing Systems*. 1057–1063.
- Christian Szegedy, Vincent Vanhoucke, Sergey Ioffe, Jon Shlens, and Zbigniew Wojna. 2016. Rethinking the inception architecture for computer vision. In *Proceedings of the IEEE conference on computer vision and pattern recognition*. 2818–2826.
- Jiaxiang Tang, Zhaoxi Chen, Xiaokang Chen, Tengfei Wang, Gang Zeng, and Ziwei Liu. 2024a. Lgm: Large multi-view gaussian model for high-resolution 3d content

- creation. In *European Conference on Computer Vision*. Springer, 1–18.
- Jiaxiang Tang, Jiawei Ren, Hang Zhou, Ziwei Liu, and Gang Zeng. 2024b. DreamGaussian: Generative Gaussian Splatting for Efficient 3D Content Creation. In *ICLR*.
- Kagan Tumer and Adrian Agogino. 2007. Distributed agent-based air traffic flow management. In *Proceedings of the 6th international joint conference on Autonomous agents and multiagent systems*. 1–8.
- Jianyuan Wang, Minghao Chen, Nikita Karaev, Andrea Vedaldi, Christian Rupprecht, and David Novotny. 2025. Vggt: Visual geometry grounded transformer. In *Proceedings of the Computer Vision and Pattern Recognition Conference*. 5294–5306.
- Zhengyi Wang, Cheng Lu, Yikai Wang, Fan Bao, Chongxuan Li, Hang Su, and Jun Zhu. 2023. Prolificdreamer: High-fidelity and diverse text-to-3d generation with variational score distillation. *Advances in neural information processing systems* 36 (2023), 8406–8441.
- David H Wolpert and Kagan Tumer. 2001. Optimal payoff functions for members of collectives. *Advances in Complex Systems* 4, 02n03 (2001), 265–279.
- Guanjun Wu, Jiemin Fang, Chen Yang, Sikuang Li, Taoran Yi, Jia Lu, Zanwei Zhou, Jiazhong Cen, Lingxi Xie, Xiaopeng Zhang, et al. 2025. Unilat3d: Geometry-appearance unified latents for single-stage 3d generation. *arXiv preprint arXiv:2509.25079* (2025).
- Jiajun Wu, Chengkai Zhang, Tianfan Xue, Bill Freeman, and Josh Tenenbaum. 2016. Learning a probabilistic latent space of object shapes via 3d generative-adversarial modeling. *Advances in neural information processing systems* 29 (2016).
- Kailu Wu, Fangfu Liu, Zhihan Cai, Runjie Yan, Hanyang Wang, Yating Hu, Yueqi Duan, and Kaisheng Ma. 2024b. Unique3d: High-quality and efficient 3d mesh generation from a single image. *Advances in Neural Information Processing Systems* 37 (2024), 125116–125141.
- Shuang Wu, Youtian Lin, Feihu Zhang, Yifei Zeng, Jingxi Xu, Philip Torr, Xun Cao, and Yao Yao. 2024a. Direct3d: Scalable image-to-3d generation via 3d latent diffusion transformer. *Advances in Neural Information Processing Systems* 37 (2024), 121859–121881.
- Jianfeng Xiang, Xiaoxue Chen, Sicheng Xu, Ruicheng Wang, Zelong Lv, Yu Deng, Hongyuan Zhu, Yue Dong, Hao Zhao, Nicholas Jing Yuan, et al. 2025a. Native and Compact Structured Latents for 3D Generation. *arXiv preprint arXiv:2512.14692* (2025).
- Jianfeng Xiang, Zelong Lv, Sicheng Xu, Yu Deng, Ruicheng Wang, Bowen Zhang, Dong Chen, Xin Tong, and Jiaolong Yang. 2025b. Structured 3d latents for scalable and versatile 3d generation. In *Proceedings of the Computer Vision and Pattern Recognition Conference*. 21469–21480.
- Haolin Xiong, Sairisheek Muttukuru, Rishi Upadhyay, Pradyumna Chari, and Achuta Kadambi. 2023. SparseSegs: Real-time 360 {deg} sparse view synthesis using gaussian splatting. *arXiv preprint arXiv:2312.00206* (2023).
- Yinghao Xu, Zifan Shi, Wang Yifan, Hansheng Chen, Ceyuan Yang, Sida Peng, Yujun Shen, and Gordon Wetzstein. 2024. Grm: Large gaussian reconstruction model for efficient 3d reconstruction and generation. In *European Conference on Computer Vision*. Springer, 1–20.
- Runjie Yan, Yinbo Chen, and Xiaolong Wang. 2025. Consistent flow distillation for text-to-3d generation. *arXiv preprint arXiv:2501.05445* (2025).
- Haitao Yang, Yuan Dong, Hanwen Jiang, Dejjia Xu, Georgios Pavlakos, and Qixing Huang. 2024. Atlas gaussians diffusion for 3d generation. *arXiv preprint arXiv:2408.13055* (2024).
- Zongxin Ye, Wenyu Li, Sidun Liu, Peng Qiao, and Yong Dou. 2024. Absgs: Recovering fine details in 3d gaussian splatting. In *Proceedings of the 32nd ACM International Conference on Multimedia*. 1053–1061.
- Zehao Yu, Anpei Chen, Binbin Huang, Torsten Sattler, and Andreas Geiger. 2024. Mip-splatting: Alias-free 3d gaussian splatting. In *Proceedings of the IEEE/CVF conference on computer vision and pattern recognition*. 19447–19456.
- Bowen Zhang, Yiji Cheng, Jiaolong Yang, Chunyu Wang, Feng Zhao, Yansong Tang, Dong Chen, and Baining Guo. 2024b. Gaussiancube: A structured and explicit radiance representation for 3d generative modeling. *arXiv preprint arXiv:2403.19655* (2024).
- Biao Zhang, Jiapeng Tang, Matthias Niessner, and Peter Wonka. 2023. 3dshape2vecset: A 3d shape representation for neural fields and generative diffusion models. *ACM Transactions On Graphics (TOG)* 42, 4 (2023), 1–16.
- Kai Zhang, Sai Bi, Hao Tan, Yuanbo Xiangli, Nanxuan Zhao, Kalyan Sunkavalli, and Zexiang Xu. 2024a. Gs-irm: Large reconstruction model for 3d gaussian splatting. In *European Conference on Computer Vision*. Springer, 1–19.
- Longwen Zhang, Ziyu Wang, Qixuan Zhang, Qiwei Qiu, Anqi Pang, Haoran Jiang, Wei Yang, Lan Xu, and Jingyi Yu. 2024c. Clay: A controllable large-scale generative model for creating high-quality 3d assets. *ACM Transactions on Graphics (TOG)* 43, 4 (2024), 1–20.
- Chen Ziwon, Hao Tan, Kai Zhang, Sai Bi, Fujun Luan, Yicong Hong, Li Fuxin, and Zexiang Xu. 2025. Long-irm: Long-sequence large reconstruction model for wide-coverage gaussian splats. In *Proceedings of the IEEE/CVF International Conference on Computer Vision*. 4349–4359.

Supplementary Material

Generative 3D Gaussians with Learned Density Control

A Evaluation Metrics

To quantitatively evaluate the quality of our generated 3D assets, we evaluate 2D renderings. For each generated asset, we render images from 8 uniformly distributed azimuth angles at a fixed elevation of 30° . The images at 45° are used as the reference images (the left-front view). We use a resolution of 512×512 for all renderings. We compare the distribution of these generated images against a reference set of images from the ground-truth test set.

To ensure a fair rendering comparison across representations and baselines, we normalize the rendered object scale before evaluation. For Gaussian assets, we set the camera radius, defined as the distance from the camera to the generated object center, to $2\times$ the maximum bounding-box extent. This is equivalent to scaling the Gaussian bounding box to 1 and rendering with radius 2. For mesh assets, including both ground-truth meshes and meshes produced by baselines, we normalize the object scale to 1 and render with radius 2. We then render all assets using a field of view of 40° .

CLIP-Score. To measure the alignment between the generated 3D assets and the input image prompts, we use the CLIP-Score metric. We employ the pre-trained CLIP ViT-L/14 model [Radford et al. 2021] to extract embeddings for both the rendered images and the text prompts. The score is calculated as the average cosine similarity between the rendered-image and reference-image embeddings across all rendered views and test samples. A higher CLIP-Score indicates better semantic alignment.

Distributional Metrics (FD and KD). We employ Fréchet Distance (FD) and Kernel Distance (KD) to assess the fidelity and diversity of the generated images compared with the real reference distribution. We use all rendered images in the Toys4K test dataset as the reference distribution, forming a reference image set of size $4,000 \times 8 = 32,000$. The generated image set also has size $4,000 \times 8 = 32,000$. We compute these metrics using two different feature extractors:

- **InceptionV3** ($FD_{\text{incep}}, KD_{\text{incep}}$): We use the standard InceptionV3 network [Szegedy et al. 2016] pretrained on ImageNet. These metrics (equivalent to FID and KID) focus on the perceptual quality and high-level semantics of the images.
- **DINOv2** ($FD_{\text{dinov2}}, KD_{\text{dinov2}}$): We use the DINOv2 ViT-L/14 model [Oquab et al. 2023] to extract features. DINOv2 features are known to capture more robust geometric and structural information, providing a complementary assessment to Inception-based metrics. We use the CLS token feature as the feature representation for each image.

B Camera Tokens

In DiT training, the model jointly predicts a camera token c_t for each object to reconstruct the camera pose of the conditioning image. Because the training camera is randomly sampled and always points toward the center of the object, we represent the camera pose using a

ALGORITHM 1: Efficient Batched Octree Sampling

```

Input: Latent code  $\mathcal{Z}$ , total samples  $P$ , max level  $L$ 
Output: Set of 3D anchor points  $\mathcal{P}_{\text{anchor}}$ , log-probabilities  $\mathcal{L}$ 
// Initialize active frontier with root cell
Initialize active frontier  $\mathcal{F}_0 \leftarrow \{(\text{root}, P, 0)\}$ ;
for  $l \leftarrow 1$  to  $L$  do
     $\mathcal{F}_l \leftarrow \emptyset$ ;
    foreach active cell  $(c_{\text{parent}}, n_{\text{parent}}, \log p_{\text{parent}}) \in \mathcal{F}_{l-1}$  do
        // Predict child distribution from latent code
        Compute logits:  $h \leftarrow \text{Model}(c_{\text{parent}}, \mathcal{Z})$ ;
        Compute probabilities:  $D \leftarrow \text{Softmax}(h)$ ;
        Compute log-probabilities:  $\log D \leftarrow \text{LogSoftmax}(h)$ ;
        // Distribute parent samples to children
        Distribute parent count  $n_{\text{parent}}$  into children counts
         $\{n_0, \dots, n_7\}$  according to  $D$  with systematic sampling;
        for  $k \leftarrow 0$  to  $7$  do
            if  $n_k > 0$  then
                // Update cumulative log-probability
                 $\log p_{\text{child}} \leftarrow \log p_{\text{parent}} + \log D[k]$ ;
                 $\mathcal{F}_l \leftarrow \mathcal{F}_l \cup \{(c_{\text{parent}} \cdot 8 + k, n_k, \log p_{\text{child}})\}$ ;
            end
        end
    end
     $\mathcal{P}_{\text{anchor}} \leftarrow \emptyset$ ;  $\mathcal{L} \leftarrow \emptyset$ ;
    // Convert leaf indices to continuous coordinates
    foreach leaf cell  $(c_{\text{leaf}}, n_{\text{leaf}}, \log p_{\text{leaf}}) \in \mathcal{F}_L$  do
        Determine spatial bounds  $B$  of cell  $c_{\text{leaf}}$ ;
        Sample  $n_{\text{leaf}}$  points  $\{x^{(j)}\}_{j=1}^{n_{\text{leaf}}} \sim \text{Uniform}(B)$ ;
         $\mathcal{P}_{\text{anchor}} \leftarrow \mathcal{P}_{\text{anchor}} \cup \{x^{(j)}\}_{j=1}^{n_{\text{leaf}}}$ ;
         $\mathcal{L} \leftarrow \mathcal{L} \cup \{\log p_{\text{leaf}}\}_{j=1}^{n_{\text{leaf}}}$ ;
    end
return  $\mathcal{P}_{\text{anchor}}, \mathcal{L}$ 

```

5D vector. The first three components of c_t encode the unit viewing direction, the fourth component is the reciprocal of the camera-to-center distance d , and the fifth component is the camera scale, computed as $d \cdot \tan(\text{fov}/2)$. Once the object is generated, this 5D camera latent is sufficient to recover the full camera pose. However, because the conditioning image is always scaled according to the alpha bounding box during both training and inference, following prior work [Xiang et al. 2025b], the predicted camera scale/distance may be inaccurate.

C Failure Cases

Our model usually reconstructs the conditioning image well, even though we do not explicitly impose a dedicated loss or inductive bias for condition-image alignment. However, the synthesized unseen views can still fail in some cases, likely due to limited generative capacity. Fig. 11 shows two representative examples. In Fig. 11(a), the generated person matches the conditioning image well in the reference view, but the back view collapses to an unrealistic dark appearance. In Fig. 11(b), the generated result is again highly consistent with the conditioning image in the reference view, while the frontal view contains an implausible head structure. We believe



Fig. 10. Camera-token visualization for randomly selected examples from the test set. The first row shows the conditioning images. The second row shows the 3D Gaussians generated by the model, rendered using the predicted camera pose recovered from the camera token. The conditioning image is always scaled according to the alpha bounding box during both training and inference, so the predicted camera scale/distance may be inaccurate.



Fig. 11. Representative failure cases of our conditional 3D Gaussian generation model. Each row shows one example. The model usually preserves strong consistency with the conditioning image in the reference view, but it may fail to synthesize plausible unseen-view geometry and appearance, leading to artifacts such as dark back views or structurally implausible results.

these failures may arise from two factors. First, the conditioning image itself is typically produced by a generative model and may not always depict a physically plausible 3D structure. Second, our model may still lack sufficient capacity to infer a fully plausible and realistic 3D structure from the input.

D Additional Comparison

We provide additional visualizations of the generation results from our method, comparing them against the TRELIS and TRELIS.2 baselines (the leading generative baselines for GS and mesh representations, respectively). As shown in Fig. 15 and Fig. 16, our approach outperforms these baselines by exhibiting better condition alignment, richer details, and more natural colors.

User Study. To further validate the perceptual quality of our method, we conducted a user study focusing on complex prompts. We collected 94 challenging image prompts and generated the corresponding 3D assets using our method (DeG), TRELIS, TRELIS.2, UniLat3D, and Hunyuan3D 2.1. The generated assets were rendered as videos to provide a comprehensive 3D view.

In the study, 32 anonymous participants were presented with 399 pairwise comparisons. In each comparison, participants viewed the same conditioning image alongside rendered videos from two different methods and were asked to choose the one with better overall quality and condition alignment. We computed Elo ratings based on these pairwise preferences. The results, summarized in Table 4, demonstrate that our method achieved a significant preference margin.

E Additional Ablations

Additional Visualizations. We visualize the generated Gaussians with different Gaussian budgets from 33K to 262K in Fig. 13. Visual quality improves as the Gaussian budget increases.

Learned Density Control Visualizations. We compare the VAE reconstruction results with and without learned density control ($\hat{\mathcal{L}}_{\text{render}}$) in Fig. 14. To validate the effectiveness of optimizing density via rendering supervision with $\hat{\mathcal{L}}_{\text{render}}$, we train a Stage-3 VAE variant that disables $\hat{\mathcal{L}}_{\text{render}}$ while keeping all other settings and training steps fixed. Incorporating $\hat{\mathcal{L}}_{\text{render}}$ allocates more Gaussian anchors to complex regions, improving fine details and avoiding missing parts. As highlighted by the red squares, the anchor point clouds show that the model without learned density control fails to allocate sufficient capacity to thin structures and intricate details, leading to blurred or fragmented geometry, whereas our full model preserves these features cleanly. This visualization complements the quantitative discussion of learned density control provided in the main text.

Table 4. User study results on 94 complex prompts. Elo ratings are computed from 399 pairwise comparisons by 32 participants. Higher Elo indicates stronger user preference.

Method	DeG (Ours)	TRELLIS	TRELLIS.2	UniLat3D	Hunyuan3D 2.1
Elo \uparrow	1137	975	992	900	<u>996</u>

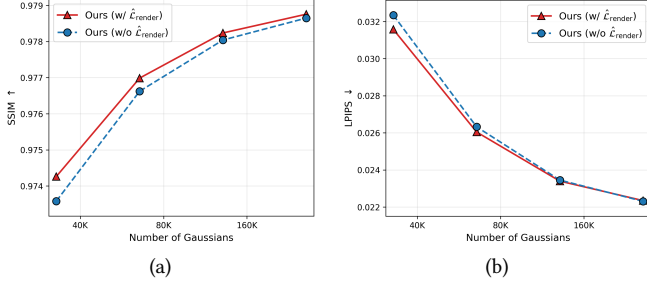


Fig. 12. Additional metrics for the learned density control setting in the main text under different Gaussian budgets: (a) SSIM \uparrow and (b) LPIPS \downarrow .

Hyperparameter Ablations. We ablate key hyperparameters of DeG-VAE, fine-tuned from the Stage 1 checkpoint for 100K steps ($P = 2048$, batch size 2). Results are reported in Table 5. For the local expansion factor K , $K = 32$ offers a good trade-off; increasing to $K = 64$ brings only marginal PSNR gain at higher cost. For the octree depth L , $L = 8$ achieves the best PSNR; $L = 10$ yields comparable quality but incurs higher training time. Removing \mathcal{L}_{reg} slightly reduces PSNR.

Additional Metrics for Learned Density Control. We additionally report SSIM and LPIPS for the same learned density control setting as in the main text; Fig. 12 visualizes the corresponding trends. Compared with the variant without $\hat{\mathcal{L}}_{\text{render}}$, enabling $\hat{\mathcal{L}}_{\text{render}}$ improves both SSIM and LPIPS in the low-budget regime, while the gap becomes small at larger Gaussian budgets, unlike PSNR. A possible explanation is that the render-loss contribution gradient is derived only from the \mathcal{L}_{11} term and may therefore underfit perceptual errors in the high-budget regime.

F Regularization

In this appendix, we provide additional details for the DeG-VAE training objective, specifically the regularization term \mathcal{L}_{reg} . \mathcal{L}_{reg} comprises three terms:

$$\mathcal{L}_{\text{reg}} = \lambda_1 \cdot \frac{1}{N} \sum_{i=1}^N \prod_{d=1}^3 \Sigma_i^d + \lambda_2 \cdot \frac{1}{N} \sum_{i=1}^N (1 - \alpha_i) + \lambda_{\text{offset}} \mathcal{L}_{\text{offset}}. \quad (18)$$

The first two terms regularize the volume and opacity of each 3D Gaussian, respectively, encouraging compact and sparse primitives. The third term $\mathcal{L}_{\text{offset}}$ enforces the spatial compactness and separation of the Gaussian clusters decoded from each anchor. We treat the set of Gaussians generated from anchor x_i as a cluster with offsets $\{\delta_{i,k}\}_{k=1}^K$. We define the cluster spread $\sigma_i = \sqrt{\frac{1}{K} \sum_{k=1}^K \|\delta_{i,k}\|^2}$ and

Table 5. Hyperparameter ablations of DeG-VAE (PSNR \uparrow , SSIM \uparrow , LPIPS \downarrow on held-out validation set from the training data, training time in GPU-hours). All variants fine-tuned from the Stage 1 checkpoint for 100K steps with $P = 2048$. \dagger marks the setting used in the main experiments and final training.

Variant	PSNR \uparrow	SSIM \uparrow	LPIPS \downarrow	Time (h)
$K = 8$	27.39	0.9383	0.0887	47.0
$K = 16$	27.40	0.9389	0.0863	47.7
$K = 32^\dagger$	<u>27.48</u>	<u>0.9398</u>	<u>0.0835</u>	47.0
$K = 64$	27.49	0.9401	0.0812	47.8
$L = 4$	27.17	0.9381	<u>0.0836</u>	45.0
$L = 6$	27.10	0.9378	0.0839	43.5
$L = 8^\dagger$	27.48	0.9398	0.0835	47.0
$L = 10$	<u>27.46</u>	<u>0.9396</u>	<u>0.0836</u>	52.6
w/o \mathcal{L}_{reg}	27.44	0.9397	0.0834	46.7
w/ $\mathcal{L}_{\text{reg}}^\dagger$	27.48	0.9398	0.0835	47.0

mean offset $\bar{\delta}_i = \frac{1}{K} \sum_{k=1}^K \delta_{i,k}$. The loss consists of two components:

$$\mathcal{L}_{\text{offset}} = \mathcal{L}_{\text{offset}}^{\text{center}} + \mathcal{L}_{\text{offset}}^{\text{sep}}. \quad (19)$$

The centering term $\mathcal{L}_{\text{offset}}^{\text{center}}$ ensures the cluster remains centered around its anchor:

$$\mathcal{L}_{\text{offset}}^{\text{center}} = \frac{1}{P} \sum_{i=1}^P \text{ReLU}(\|\bar{\delta}_i\| - \gamma \sigma_i), \quad (20)$$

where $\gamma = 0.5$ is a hyperparameter controlling the permissible drift. The separation term $\mathcal{L}_{\text{offset}}^{\text{sep}}$ prevents cluster overlap by constraining the spread to be smaller than the distance to other anchors:

$$\mathcal{L}_{\text{offset}}^{\text{sep}} = \frac{1}{P^2} \sum_{i=1}^P \sum_{j \neq i}^P \text{ReLU}(\sigma_i - \|x_i - x_j\|). \quad (21)$$

G Octree Sampling Algorithm

We provide our implementation of the efficient octree sampling algorithm in Alg. 1. We use this algorithm to sample P anchor points from stochastic density decoder q_θ at inference time.

H Primitive-Level Implementation of the render loss contribution gradient

Setup. Following the main paper, we first sample P anchors, and each anchor x_a spawns K Gaussian primitives $\{g_{a,k}\}_{k=1}^K$ via local expansion. We extend the rasterizer used in Mip-Splatting [Yu et al. 2024] with render loss contribution gradient computation. The rasterizer itself does not operate on anchors; it only receives the flattened primitive set

$$\mathcal{G} = \{g_i\}_{i=1}^N, \quad N = P \cdot K, \quad (22)$$

where each flattened index i corresponds to some anchor-primitive pair (a, k) . Let

$$I = \mathcal{R}(\mathcal{G}, \pi) \in \mathbb{R}^{C \times H \times W} \quad (23)$$

be the rendered image. In this section, we focus on the \mathcal{L}_{11} term inside the render loss $\mathcal{L}_{\text{render}}$. During training, all K primitives generated from the same anchor share the same anchor probability $q_{\theta}(x_a | \mathcal{Z})$ when constructing the density-learning signal. The residual at pixel p in channel c is

$$R_{p,c} = I_{p,c} - I_{p,c}^{\text{GT}}, \quad (24)$$

computed once after the forward pass and stored for the backward pass.

Target Quantity. For each Gaussian primitive g_i we want the quantity

$$\Delta \mathcal{L}_{11,i} = \mathcal{L}_{11}(I, I^{\text{GT}}) - \mathcal{L}_{11}(I^{(-i)}, I^{\text{GT}}), \quad (25)$$

where $I^{(-i)}$ is the image that would be rendered if g_i were absent. Computing (25) naively requires N additional forward passes. Instead, we derive an efficient implementation that computes this quantity for all Gaussians **within a standard forward and backward pass**, with negligible overhead. The resulting contributions are then associated with the shared anchor probability of the source anchor.

Color change from removing one primitive. Standard alpha compositing renders pixel p as

$$I_{p,c} = \sum_i T_{p,i} \alpha_{p,i} c_{i,c} + T_{p,\text{final}} b_c, \quad (26)$$

where $T_{p,i} = \prod_{j<i} (1 - \alpha_{p,j})$ is the transmittance just before primitive i , $\alpha_{p,i}$ is its blending weight, $c_{i,c}$ is its color, and b_c is the background color.

If g_i is removed, the pixel color changes by

$$\Delta C_{p,i,c} = T_{p,i} \alpha_{p,i} (c_{i,c} - \text{back}_{p,i,c}), \quad (27)$$

In a standard backward pass, both the transmittance $T_{p,i}$ and the back color $\text{back}_{p,i,c}$ are already accumulated, so this color change can be computed efficiently for every primitive at negligible extra cost. Here, $\text{back}_{p,i,c}$ denotes the blended color already accumulated behind g_i in the original rasterizer, i.e. the color that would be seen from layers deeper than g_i .

Per-pixel L1 change. The change in the per-pixel, per-channel L1 loss when g_i is removed is

$$\delta_{p,i,c}^{\text{L1}} = |R_{p,c}| - |R_{p,c} - \Delta C_{p,i,c}|. \quad (28)$$

Summing over all pixels and channels gives the primitive-level contribution of g_i :

$$\Delta \mathcal{L}_{11,i} = \sum_p \sum_c \delta_{p,i,c}^{\text{L1}}. \quad (29)$$

Fused CUDA implementation. The standard backward pass already iterates over all (primitive, pixel) pairs in reverse depth order to compute gradients with respect to Gaussian parameters. We accumulate $\Delta \mathcal{L}_{11,i}$ inside this same loop at negligible extra cost. At each step the backward pass maintains the transmittance $T_{p,i}$ (unwound from the final transmittance) and the accumulated background color $\text{back}_{p,i,c}$

Table 6. Quantitative VAE reconstruction results for the tested token-length and Gaussian-budget sweeps. We vary token length with a fixed Gaussian budget of 262K, and vary Gaussian budget with a fixed token length of 8192.

(a) Token-length sweep with fixed Gaussian budget 262K.

Token length	PSNR \uparrow	SSIM \uparrow	LPIPS \downarrow
1024	34.94	0.9750	0.0265
2048	35.46	0.9770	0.0243
4096	35.74	0.9781	0.0230
8192	35.89	0.9788	0.0223

(b) Gaussian-budget sweep with fixed token length 8192.

# Gaussians	PSNR \uparrow	SSIM \uparrow	LPIPS \downarrow
33K	34.73	0.9743	0.0316
66K	35.45	0.9770	0.0260
131K	35.77	0.9782	0.0234
262K	35.89	0.9788	0.0223

(built up from the back of the scene). These two quantities are exactly what Eq. (27) requires, so computing $\Delta C_{p,i,c}$ and the resulting $\delta_{p,i,c}^{\text{L1}}$ adds only a few arithmetic operations per (primitive, pixel, channel) triple. The per-primitive sum $\Delta \mathcal{L}_{11,i}$ is accumulated via an atomic add into a buffer of length N . Outside the rasterizer, each primitive contribution is paired with the probability of its source anchor; hence all K primitives expanded from the same anchor reuse the same factor $q_{\theta}(x_a | \mathcal{Z})$ in the density-learning objective.

Reward Clamping. In our experiments, we apply a simple clamping rule to improve the performance of the density-learning signal from the render loss contribution gradient. After accumulating anchor-level contributions, we apply two clamping operations. First, we compute the 10th-percentile threshold and clamp the smallest 10% of contributions to this threshold value. Second, we clamp positive contributions, i.e., contributions with $\text{renderlosscontributiongradient} > 0$, to zero. This keeps the update focused on locations where the presence of an anchor leads to a larger reduction in rendering loss, while avoiding high-variance outliers.

Scope and Limitation. This implementation only considers the \mathcal{L}_{11} component of the render loss $\mathcal{L}_{\text{render}}$. Perceptual terms such as LPIPS are not pixel-wise losses, so assigning an exact per-primitive contribution inside the rasterizer is difficult. Therefore, this section only computes the contribution with respect to the main rendering \mathcal{L}_{11} term.

I Effect of Token Count and Gaussian Budget on VAE Reconstructions

We provide a qualitative comparison of VAE reconstructions for two controlled sweeps. In the first sweep, we vary the token length while fixing the Gaussian budget to 262K. In the second sweep, we vary the Gaussian budget while fixing the token length to 8192. We report PSNR \uparrow , SSIM \uparrow , and LPIPS \downarrow on the Toys4K dataset in Table 6.

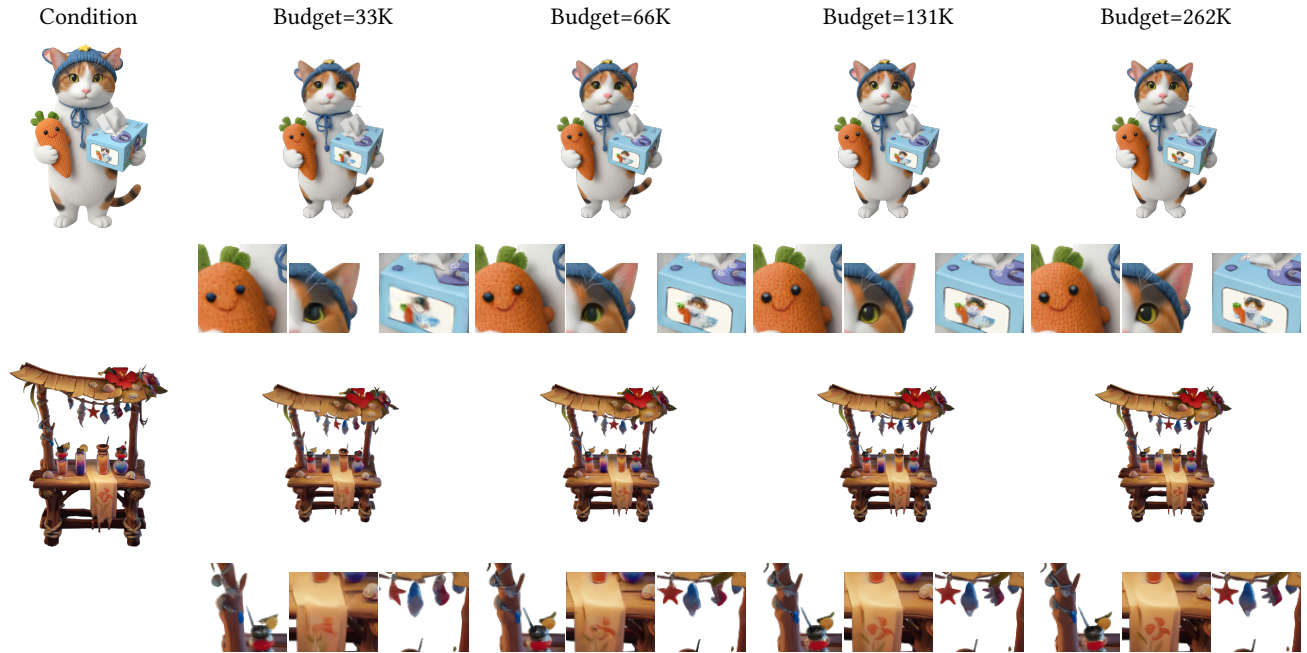


Fig. 13. Visualizations under different Gaussian budgets, ranging from 33K to 262K. For each rendering, three zoomed-in crops are shown beneath the full image. Each row corresponds to the same generated latent decoded with a different Gaussian budget.

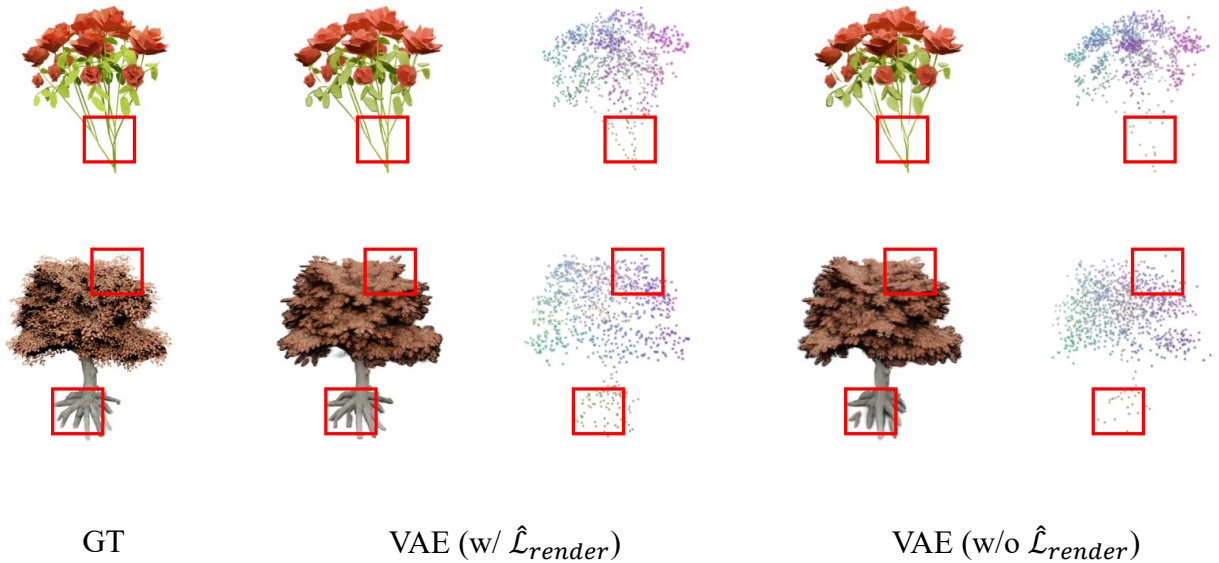


Fig. 14. Visual comparison of VAE reconstruction with and without learned density control ($\hat{\mathcal{L}}_{render}$). The Gaussian budget is set to 33K. The anchor point clouds are shown alongside the rendered images. Red squares highlight regions where learned density control successfully allocates more Gaussian anchors to preserve fine details and prevent missing structures.

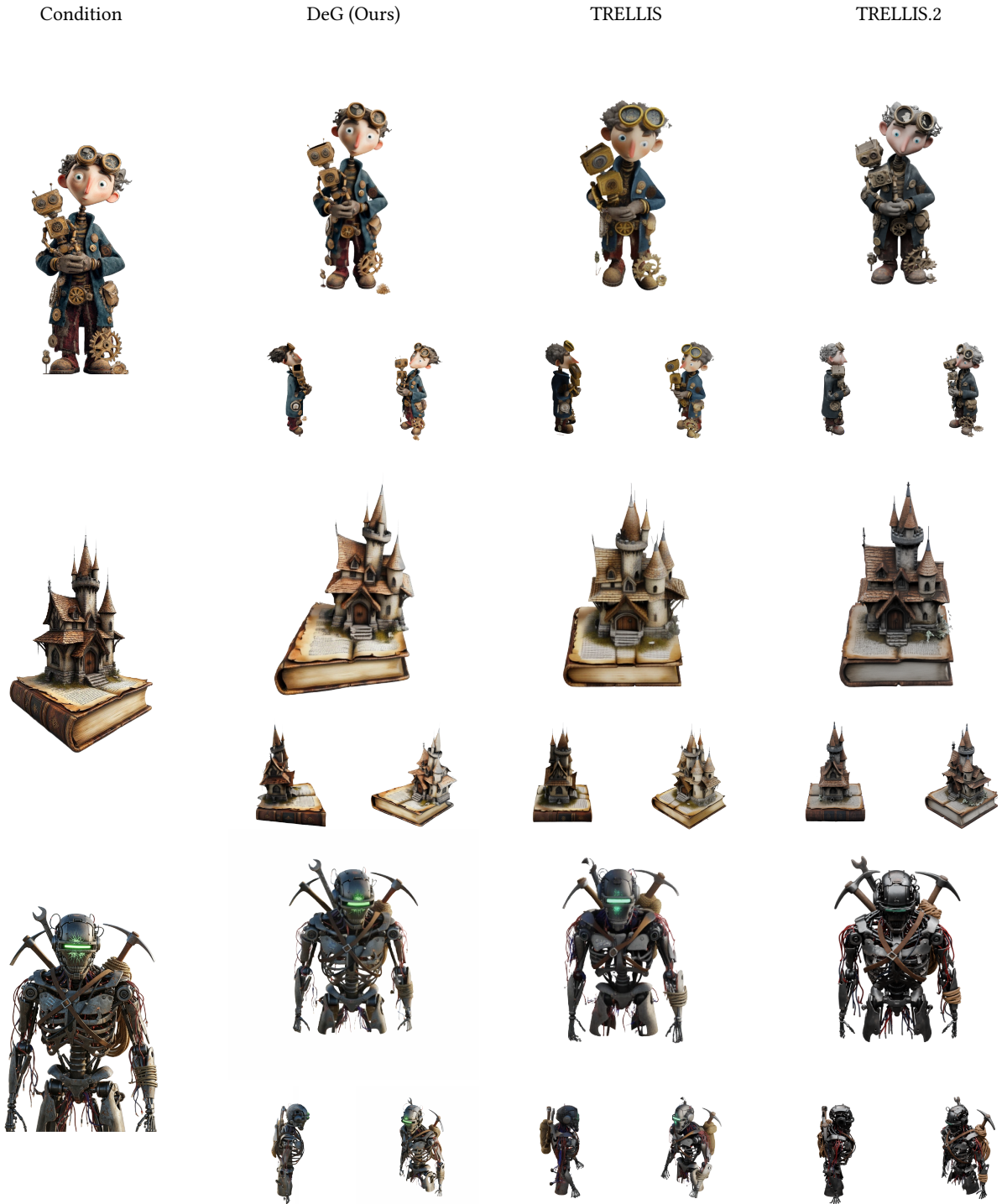


Fig. 15. Additional visualizations of the generation results. DeG and TRELLIS are shown with Gaussian rendering, while TRELLIS-2 is shown with mesh rendering. Our method demonstrates better condition alignment, richer details, and more natural colors compared with the baselines. The Gaussian count for our method (DeG) is 262K. The Gaussian counts for TRELLIS are 360K, 456K, and 459K from top to bottom, respectively.



Fig. 16. Additional visualizations of the generation results. DeG and TRELLIS are shown with Gaussian rendering, while TRELLIS-2 is shown with mesh rendering. Our method demonstrates better condition alignment, richer details, and more natural colors compared with the baselines. The Gaussian count for our method (DeG) is 262K. The Gaussian counts for TRELLIS are 776K, 912K, and 907K from top to bottom, respectively.